Monthly Notices of the ROYAL ASTRONOMICAL SOCIETY

MNRAS **517,** 4590–4606 (2022) https://doi.org/10.1093/mnras/stac2136
Advance Access publication 2022 August 1

Abundance analysis of APOGEE spectra for 58 metal-poor stars from the bulge spheroid

R. Razera [1]★ B. Barbuy [1]★ T. C. Moura [1] H. Ernandes [1] A. Pérez-Villegas [2] S. O. Souza [1,3] C. Chiappini [3]★ A. B. A. Queiroz [3,4] F. Anders [5] J. G. Fernández-Trincado [6] A. C. S. Friaça,[1] K. Cunha [7,8] V. V. Smith [9] B. X. Santiago [10] R. P. Schiavon [11] M. Valentini [3] D. Minniti [12,13] M. Schultheis [14] D. Geisler [15,16,17] J. Sobeck [18] V. M. Placco [9] and M. Zoccali [19,20]

[1]*IAG, Universidade de São Paulo, Rua do Matão 1226, Cidade Universitária, São Paulo 05508-900, Brazil*
[2]*Instituto de Astronomía, Universidad Nacional Autónoma de México, A. P. 106, C.P. 22800, Ensenada, B. C., México*
[3]*Leibniz-Institut für Astrophysik Potsdam (AIP), An der Sternwarte 16, D-14482 Potsdam, Germany*
[4]*Institut für Physik und Astronomie, Universität Potsdam, Haus 28 Karl-Liebknecht-Str 24/25, D-14476 Golm (Potsdam), Germany*
[5]*Institut de Ciències del Cosmos, Universitat de Barcelona (IEEC-UB), Martí i Franquès 1, E-08028 Barcelona, Spain*
[6]*Instituto de Astronomía, Universidad Católica del Norte, Av. Angamos 0610, Antofagasta, Chile*
[7]*University of Arizona, Tucson, AZ 85719, USA*
[8]*Observatório Nacional, S Cristóvão, Rio de Janeiro, Brazil*
[9]*NSF's NOIRLab, 950 N. Cherry Ave., Tucson, AZ 85719, USA*
[10]*Universidade Federal do Rio Grande do Sul, Caixa Postal 15051, 91501-970 Porto Alegre, Brazil*
[11]*Astrophysics Research Institute, Liverpool John Moores University, Liverpool, L3 5RF, UK*
[12]*Instituto de Astrofísica, Facultad de Ciencias Exactas, Universidad Andres Bello, Fernández Concha 700, Las Condes, Santiago, Chile*
[13]*Vatican Observatory, Vatican City State I-00120, Italy*
[14]*Observatoire de la Côte d'Azur, CNRS, Laboratoire Lagrange, Université Côte d'Azur, F- 06108 Nice, France*
[15]*Departamento de Astronomia, Universidad de Concepción, Casilla 160-C, Concepción, Chile*
[16]*Instituto de Investigación Multidisciplinario en Ciencia y Tecnología, Universidad de La Serena, Avenida Raúl Bitrán S/N, La Serena, Chile*
[17]*Departamento de Astronomía, Facultad de Ciencias, Universidad de La Serena, Av. Juan Cisternas 1200, La Serena, Chile*
[18]*Department of Astronomy, University of Washington, Box 351580, Seattle, WA 98195, USA*
[19]*Instituto de Astrofísica, Pontificia Universidad Católica de Chile, Casilla 306, Santiago 22, Chile*
[20]*Millenium Institute of Astrophysics (MAS), Nuncio Monseñor Sótero Sanz 100, Providencia, Santiago Chile*

Accepted 2022 July 26. Received 2022 July 26; in original form 2022 June 24

ABSTRACT

The central part of the Galaxy hosts a multitude of stellar populations, including the spheroidal bulge stars, stars moved to the bulge through secular evolution of the bar, inner halo, inner thick disc, inner thin disc, as well as debris from past accretion events. We identified a sample of 58 candidate stars belonging to the stellar population of the spheroidal bulge, and analyse their abundances. The present calculations of Mg, Ca, and Si lines are in agreement with the ASPCAP abundances, whereas abundances of C, N, O, and Ce are re-examined. We find normal α-element enhancements in oxygen, similar to magnesium, Si, and Ca abundances, which are typical of other bulge stars surveyed in the optical in Baade's Window. The enhancement of [O/Fe] in these stars suggests that they do not belong to accreted debris. No spread in N abundances is found, and none of the sample stars is N-rich, indicating that these stars are not second generation stars originated in globular clusters. Ce instead is enhanced in the sample stars, which points to an s-process origin such as due to enrichment from early generations of massive fast rotating stars, the so-called spinstars.

Key words: stars: abundances – stars: atmospheres – Galaxy: bulge.

1 INTRODUCTION

The stellar populations in the central part of the Galaxy can inform us about its complex formation processes. This region was recently confirmed to contain stars in a metal-poor spheroidal bulge (e.g. Babusiaux et al. 2010; Dékány et al. 2013; Babusiaux 2016; Zoccali, Valenti & Gonzalez 2018; Arentsen et al. 2020; Kunder et al. 2020; Savino et al. 2020; Queiroz et al. 2021 and references therein), along with a metal-rich contribution from the bar and inner thin disc, thick disc, and halo interlopers. In addition, debris of past accretion events, such as *Gaia*-Enceladus-Sausage (GES) (Belokurov et al. 2018; Helmi et al. 2018), and many other dwarf galaxy remnants, and minor substructures absorbed during the early stages of the Galaxy formation (see e.g. Horta et al. 2020, 2021, 2022; Fernández-Trincado et al. 2022) are present. Therefore studies of the Galactic bulge region are important for understanding the early stages of our Galaxy's formation (e.g. Barbuy, Chiappini & Gerhard 2018a; Rojas-Arriagada et al. 2020). In particular, Queiroz et al. (2020,

★ E-mail: roberta.razera@usp.br (RR); b.barbuy@iag.usp.br (BB); cristina.chiappini@aip.de (CC)

2021) combining distance derivation with proper motions from the *Gaia* Early Data Release 3 (Gaia Collaboration et al. 2021) revealed stars of large eccentricity, but with orbits confined to the bulge region – with a maximum height from the Galactic mid-plane, $|z|_{\rm max}$, below 3 kpc with intermediate metallicities, which are good candidates for belonging to the oldest Galactic bulge component (which we here call spheroid bulge stars).

The spheroidal metal-poor bulge can be thought of as a pressure supported structure formed through violent processes, such as hierarchical clustering via minor mergers at a very early stage of the Galaxy. Ferraro et al. (2021) finds evidence that clumps of stars and gas existed at the time of the Milky Way formation. *N*-body simulations assume instead that early stellar discs heat rapidly as they form, and can lead to different density distributions for metal-rich and metal-poor stars (e.g. Debattista et al. 2017). Many other options are possible to form the metal-poor spheroid such as a major merger accretion of dwarf galaxies among others (e.g. Barbuy et al. 2018a). Whatever process it leads to an observed metal-poor spheroid, and it has also to explain the very old ages of the *in situ* globular clusters such as e.g. HP 1 (Kerber et al. 2019), Djorgovski 2 (Ortolani et al. 2019), Palomar 6 (Souza et al. 2021) of ages derived to be of 12.8 ± 0.9, 12.7 ± 0.7, and 12.4 ± 0.9 Gyr, respectively.

The search for the earliest stars in the Galaxy is an important endeavour to try to identify the earliest chemical abundances imprinted in the oldest stars, and the nature of the supernovae that enriched them. Most of the current observational efforts in finding the chemical imprints left by the first stars have focused on the most metal-poor stars found in the Milky Way halo (Beers & Christlieb 2005; Beers et al. 2017). Very metal-poor stars were also found in ultra-faint dwarf galaxies, which are intriguing dark matter dominated objects with very low average metallicities (Ji et al. 2016). The Galactic bulge, as well as the halo, is a potential host of some of the oldest stars in our Galaxy. Tumlinson (2010) suggests that half of the oldest stars were formed in the central parts of the Galaxy. Searches for field metal-poor stars in the Galactic bulge are the target of surveys such as those by Howes et al. (2016), Casey & Schlaufman (2015), the Pristine Inner Galaxy Survey (PIGS, Arentsen et al. 2020), HERBS (Duong et al. 2019a, Duong et al. 2019b), and COMBS (Lucey et al. 2019, 2021, 2022) surveys. Metal-poor stars in the Galactic bulge have been mostly traced by Globular clusters (Rossi et al. 2015; Bica, Ortolani & Barbuy 2016) and RR Lyrae stars (Minniti et al. 2017), which show a peak at [Fe/H] ~ -1.0 (Barbuy et al. 2018a). This metallicity peak at [Fe/H] ~ -1.0 has been also recently confirmed regarding field stars by Lucey et al. (2021). In fact, it is expected that a fast chemical enrichment in the Galactic bulge results in a very old population with this relatively high metallicity that would correspond to the age of stars with [Fe/H] ~ -3.0 in the halo (Chiappini et al. 2011; Wise et al. 2012; Barbuy et al. 2018a).

Our main interest in the present work is to analyse the abundances of stars of the spheroidal bulge with a moderate metallicity of [Fe/H] < -0.8, in order to try to identify the earliest supernovae of the central regions of the Galaxy, and imposing constraints on the early chemical enrichment of the Milky Way. For the selection of sample stars, we applied kinematical and dynamical criteria by combining data from Apache Point Observatory Galactic Evolution Experiment (APOGEE) and *Gaia* Early Data Release EDR3. We chose stars with azimuthal velocity $V_\phi < 0$ (this selection will avoid contamination by disc stars, but would still include accreted debris of objects such as GES) that have orbits confined within 4 kpc of the Galactic centre, a maximum height of $|z|_{\rm max} < 3.0$ kpc, eccentricity > 0.7 and with orbits not supporting the bar structure. With this selection, as noted above, we expect our sample to be dominated by a pressure supported, most probably old component of the bulge. We hope to discard the contamination of our sample by accreted debris, thanks to the detailed chemical information and, in particular, the alpha-over-iron enhancement expected to be low in most of the accreted debris. Finally, given that we used a barred potential, the z-component of angular momentum (L_z) is not conserved, and most orbits are either retrograde or prograde, and a fraction among those identified as counter-rotating keep retrograde along its orbit.

In this paper, we carried out an analysis of atomic and molecular lines for the selected sample of 58 metal-poor spheroid bulge star candidates aiming at refining the APOGEE Stellar Parameter and Chemical Abundance Pipeline (ASPCAP; García-Pérez et al. 2016) results, in order to interpret the derived abundances in terms of the early chemo-dynamical evolution of the bulge. As it will be shown, this re-analysis is critical for some alpha elements, and therefore for the identification and confirmation of old spheroid bulge stars at moderately low metallicities. In the present work, we adopt the stellar parameters issued from the DR17 release of the ASPCAP code. The C, N, and O abundances are derived from CO, OH, and CN lines that are interdependent and since there are such molecular lines all over the spectra, they can affect the abundances of atomic lines. We also refine the abundances of Ce. Other elements including Na, Al, and iron-peak elements will be the topic of a future work.

In Section 2, the selection of our sample is described. The element abundances are derived in Section 3. In Section 4, the results are compared with literature data for bulge samples and chemodynamical models, and discussed. In Section 5, conclusions are drawn.

2 THE SAMPLE

APOGEE (Majewski, Schiavon & Frinchaboy 2017) is part of the Sloan Digital Sky Survey III and IV (SDSS; Blanton et al. 2017). It is a project encompassing spectroscopic programs that observe Milky Way stars at high-resolution and high signal-to-noise ratios (S/N) in the near-infrared (NIR). The project SDSS-IV technical summary, the SDSS telescope and APOGEE spectrograph are described in Blanton et al. (2017), Gunn et al. (2006), and Wilson et al. (2019), respectively, whereas Zasowski et al. (2013, 2017), Beaton et al. (2021), and Santana et al. (2021) describe the APOGEE and APOGEE-2 Target Selections. The data release 17 (DR17) contains high-resolution (R $\sim$ 22 500) NIR spectra (15140–16940 Å) for some 7×10^5 stars, covering both the northern and southern sky. While APOGEE-1 observed the Milky Way bulge/bar at $l > 0$ deg, APOGEE-2 covers the whole bulge/bar region.

Given that the central part of the Milky Way hosts members of all Galactic components, including the bulge, disc, and halo (Pérez-Villegas et al. 2020; Rojas-Arriagada et al. 2020; Queiroz et al. 2021), we have used the chemo-orbital analysis shown in Queiroz et al. (2021) to identify good candidates in the spheroidal bulge APOGEE sample. To disentangle the different stellar populations coexisting in the innermost parts of the Galaxy is not an easy task, and one of the difficulties is to compute precise distances for these stars due to the high extinction. Thanks to StarHorse (Santiago et al. 2016; Queiroz et al. 2018), precise stellar distances for the entire APOGEE sample were derived both for DR16 (Ahumada et al. 2020; Queiroz et al. 2020) and DR17[1] (Abdurro'uf et al. 2022; Queiroz et al. 2022, in preparation).

We selected stars from the reduced-proper-motion (RPM) sample of Queiroz et al. (2021). For that sample, orbits were calculated using

[1] Value added catalogues are available in both releases.

Table 1. Coordinates, Starshorse distances, *Gaia* EDR3 proper motions, *Gaia* DR2 radial velocities, and orbital parameters for the selected 58 stars from RPM sample of Queiroz et al. (2021).

ID	α (°)	δ (°)	$d_\odot$ (kpc)	μ^*_α (mas yr^{-1})	μ_δ (mas yr^{-1})	RV (km s^{-1})	r_{min} (kpc)	r_{max} (kpc)	$\|z\|_{max}$ (kpc)	e
2M17153858-2759467	258.911	−27.996	8.51 ± 0.50	−5.46 ± 0.02	−5.30 ± 0.02	191.79 ± 0.01	0.13 ± 0.05	2.51 ± 0.46	1.68 ± 0.18	0.90 ± 0.04
2M17173248-2518529	259.385	−25.315	7.79 ± 0.91	−2.14 ± 0.04	−9.47 ± 0.03	187.54 ± 0.02	0.19 ± 0.16	3.73 ± 0.79	2.34 ± 0.49	0.91 ± 0.05
2M17173693-2806495	259.404	−28.114	6.94 ± 0.45	−4.85 ± 0.03	−9.80 ± 0.02	−104.63 ± 0.01	0.12 ± 0.06	1.94 ± 0.44	1.52 ± 0.19	0.89 ± 0.05
2M17190320-2857321	259.763	−28.959	6.81 ± 0.46	−5.95 ± 0.03	−7.60 ± 0.02	−83.87 ± 0.03	0.14 ± 0.07	1.80 ± 0.33	0.74 ± 0.26	0.87 ± 0.05
2M17224443-2343053	260.685	−23.718	6.02 ± 0.42	−9.20 ± 0.02	−8.15 ± 0.01	114.23 ± 0.01	0.21 ± 0.12	3.87 ± 0.51	2.61 ± 0.23	0.89 ± 0.07
2M17250290-2800385	261.262	−28.011	5.83 ± 0.76	−3.05 ± 0.03	−9.26 ± 0.02	26.27 ± 0.01	0.20 ± 0.11	2.63 ± 0.71	1.02 ± 0.38	0.85 ± 0.07
2M17265563-2813558	261.732	−28.232	7.55 ± 0.56	−7.25 ± 0.04	−7.31 ± 0.03	196.52 ± 0.03	0.13 ± 0.07	2.40 ± 0.53	1.52 ± 0.36	0.91 ± 0.04
2M17281191-2831393	262.050	−28.528	6.50 ± 0.58	−9.70 ± 0.03	−4.61 ± 0.02	81.01 ± 0.02	0.14 ± 0.05	2.24 ± 0.68	1.87 ± 0.29	0.90 ± 0.05
2M17285088-2855427	262.212	−28.929	7.59 ± 0.42	−4.80 ± 0.03	−5.57 ± 0.02	−7.43 ± 0.01	0.06 ± 0.03	0.83 ± 0.25	0.47 ± 0.02	0.87 ± 0.04
2M17291778-2602468	262.324	−26.046	6.93 ± 0.44	−5.60 ± 0.06	−7.06 ± 0.04	−47.65 ± 0.01	0.12 ± 0.07	1.50 ± 0.43	0.66 ± 0.10	0.86 ± 0.07
2M17292082-2126433	262.337	−21.445	6.60 ± 0.68	−0.84 ± 0.02	−10.79 ± 0.02	−79.08 ± 0.01	0.19 ± 0.10	2.83 ± 0.67	2.06 ± 0.14	0.87 ± 0.09
2M17293482-2741164	262.395	−27.688	6.81 ± 0.52	−3.56 ± 0.04	−8.16 ± 0.03	−74.26 ± 0.02	0.09 ± 0.06	1.51 ± 0.39	0.59 ± 0.10	0.89 ± 0.05
2M17295481-2051262	262.478	−20.857	7.00 ± 0.38	0.11 ± 0.04	−6.20 ± 0.03	−213.15 ± 0.04	0.16 ± 0.08	3.43 ± 0.40	2.31 ± 0.08	0.90 ± 0.04
2M17301495-2337002	262.562	−23.617	8.28 ± 0.66	−8.24 ± 0.04	−9.11 ± 0.02	−70.19 ± 0.01	0.24 ± 0.17	1.97 ± 0.93	1.81 ± 0.32	0.83 ± 0.17
2M17303581-2354453	262.649	−23.913	7.99 ± 0.60	−8.31 ± 0.04	−4.45 ± 0.02	27.88 ± 0.01	0.10 ± 0.14	1.52 ± 0.40	1.38 ± 0.18	0.87 ± 0.08
2M17310874-2956542	262.786	−29.948	6.81 ± 0.00	−3.38 ± 0.04	−7.93 ± 0.03	−10.11 ± 0.02	0.19 ± 0.01	1.50 ± 0.01	0.36 ± 0.00	0.77 ± 0.01
2M17323787-2023013	263.158	−20.384	7.76 ± 0.55	−5.22 ± 0.03	−1.34 ± 0.02	−97.24 ± 0.01	0.17 ± 0.08	2.53 ± 0.24	1.62 ± 0.22	0.88 ± 0.06
2M17324257-2301417	263.177	−23.028	7.69 ± 0.74	−2.70 ± 0.05	−7.92 ± 0.03	−181.81 ± 0.01	0.16 ± 0.13	1.67 ± 0.58	1.27 ± 0.28	0.83 ± 0.09
2M17330695-2302130	263.279	−23.037	7.40 ± 0.10	−3.51 ± 0.04	−9.38 ± 0.03	6.42 ± 0.00	0.11 ± 0.05	1.44 ± 0.04	0.95 ± 0.01	0.86 ± 0.05
2M17330730-2407378	263.280	−24.127	5.32 ± 0.25	−4.74 ± 0.03	−8.85 ± 0.02	−31.23 ± 0.01	0.11 ± 0.04	3.15 ± 0.25	1.41 ± 0.42	0.93 ± 0.03
2M17341796-3905103	263.575	−39.086	8.63 ± 0.69	−2.19 ± 0.07	−3.37 ± 0.05	3.77 ± 0.03	0.23 ± 0.06	1.90 ± 0.22	0.65 ± 0.27	0.78 ± 0.05
2M17342067-3902066	263.586	−39.035	9.80 ± 0.00	−2.51 ± 0.08	−3.17 ± 0.06	5.95 ± 0.04	0.13 ± 0.05	2.50 ± 0.14	1.50 ± 0.18	0.90 ± 0.04
2M17344841-4540171	263.702	−45.671	6.71 ± 0.38	−0.85 ± 0.02	−6.51 ± 0.01	148.00 ± 0.01	0.17 ± 0.15	3.67 ± 0.51	2.61 ± 0.18	0.91 ± 0.09
2M17351981-1948329	263.833	−19.809	8.20 ± 0.32	−2.39 ± 0.02	−6.57 ± 0.01	−230.13 ± 0.00	0.36 ± 0.23	2.61 ± 0.53	2.14 ± 0.16	0.77 ± 0.16
2M17354093-1716200	263.921	−17.272	6.15 ± 0.35	−4.18 ± 0.02	−7.53 ± 0.01	−84.29 ± 0.01	0.17 ± 0.11	2.84 ± 0.27	1.59 ± 0.16	0.88 ± 0.06
2M17382504-2424163	264.604	−24.405	6.78 ± 0.52	−2.34 ± 0.07	−8.58 ± 0.04	−56.51 ± 0.01	0.12 ± 0.09	1.68 ± 0.43	0.66 ± 0.08	0.87 ± 0.10
2M17390801-2331379	264.783	−23.527	7.57 ± 0.54	−7.05 ± 0.03	−3.91 ± 0.02	−199.67 ± 0.01	0.13 ± 0.07	1.92 ± 0.36	1.43 ± 0.17	0.88 ± 0.05
2M17392719-2310311	264.863	−23.175	6.70 ± 0.31	−10.26 ± 0.03	−7.39 ± 0.02	47.66 ± 0.00	0.13 ± 0.07	2.67 ± 0.47	1.90 ± 0.22	0.90 ± 0.04
2M17453659-2309130	266.402	−23.154	6.31 ± 0.56	−4.98 ± 0.23	−7.39 ± 0.15	−140.43 ± 0.02	0.12 ± 0.04	2.21 ± 0.47	0.54 ± 0.32	0.90 ± 0.05
2M17473299-2258254	266.887	−22.974	7.36 ± 0.61	−4.18 ± 0.02	−9.24 ± 0.01	−39.26 ± 0.01	0.11 ± 0.04	1.37 ± 0.35	0.44 ± 0.04	0.87 ± 0.05
2M17482995-2305299	267.125	−23.092	7.05 ± 0.43	−0.95 ± 0.03	−6.72 ± 0.02	−216.54 ± 0.02	0.14 ± 0.06	2.07 ± 0.51	0.73 ± 0.32	0.87 ± 0.06
2M17483633-2242483	267.151	−22.713	8.11 ± 0.69	−0.62 ± 0.03	−9.74 ± 0.02	−93.04 ± 0.00	0.12 ± 0.07	1.38 ± 0.61	0.87 ± 0.34	0.85 ± 0.09
2M17503065-2313234	267.628	−23.223	6.83 ± 0.38	−4.88 ± 0.05	−6.57 ± 0.03	−203.16 ± 0.01	0.09 ± 0.03	1.94 ± 0.42	0.37 ± 0.13	0.92 ± 0.03
2M17503263-3654102	267.636	−36.903	7.49 ± 0.62	−7.00 ± 0.02	−4.97 ± 0.01	11.58 ± 0.01	0.10 ± 0.05	1.51 ± 0.38	1.28 ± 0.08	0.89 ± 0.04
2M17511568-3249403	267.815	−32.828	7.54 ± 0.59	−4.58 ± 0.04	−9.25 ± 0.03	−102.21 ± 0.01	0.08 ± 0.03	1.28 ± 0.21	0.45 ± 0.03	0.88 ± 0.04
2M17532599-2053304	268.358	−20.892	7.66 ± 0.59	−3.44 ± 0.04	−7.77 ± 0.03	−78.10 ± 0.01	0.08 ± 0.04	1.39 ± 0.22	0.42 ± 0.05	0.89 ± 0.04
2M17552681-3334272	268.862	−33.574	7.67 ± 0.55	−3.57 ± 0.03	−4.88 ± 0.02	166.48 ± 0.02	0.09 ± 0.03	1.43 ± 0.25	0.65 ± 0.04	0.89 ± 0.04
2M17552744-3228019	268.864	−32.467	7.10 ± 0.89	−7.00 ± 0.03	−6.81 ± 0.02	−71.82 ± 0.01	0.10 ± 0.05	1.34 ± 0.68	0.81 ± 0.24	0.88 ± 0.06
2M18005152-2916576	270.215	−29.283	8.45 ± 0.60	1.18 ± 0.04	−9.34 ± 0.03	−77.43 ± 0.02	0.17 ± 0.09	1.25 ± 0.61	1.07 ± 0.34	0.80 ± 0.10
2M18010424-3126158	270.268	−31.438	7.10 ± 0.57	−1.22 ± 0.03	−9.10 ± 0.02	81.96 ± 0.00	0.09 ± 0.04	1.43 ± 0.50	0.82 ± 0.15	0.88 ± 0.06
2M18020063-1814495	270.503	−18.247	5.97 ± 0.38	−4.65 ± 0.05	−8.19 ± 0.04	−94.07 ± 0.02	0.11 ± 0.03	2.85 ± 0.40	0.55 ± 0.44	0.92 ± 0.02
2M18023156-2834451	270.632	−28.579	8.15 ± 0.44	−4.55 ± 0.07	−10.32 ± 0.05	−190.17 ± 0.01	0.27 ± 0.10	1.59 ± 0.40	0.62 ± 0.33	0.73 ± 0.12
2M18042687-2928348	271.112	−29.476	7.89 ± 0.75	−2.34 ± 0.03	−7.82 ± 0.02	−113.51 ± 0.02	0.08 ± 0.06	1.05 ± 0.41	0.61 ± 0.07	0.89 ± 0.07
2M18044663-3132174	271.194	−31.538	7.31 ± 0.43	−6.68 ± 0.03	−7.25 ± 0.02	−145.20 ± 0.01	0.10 ± 0.04	1.62 ± 0.30	1.10 ± 0.14	0.89 ± 0.05
2M18050452-3249149	271.269	−32.821	5.51 ± 0.41	−3.19 ± 0.02	−10.36 ± 0.01	46.90 ± 0.01	0.12 ± 0.06	3.58 ± 0.59	1.47 ± 0.51	0.93 ± 0.04
2M18050663-3005419	271.278	−30.095	7.92 ± 0.36	−1.98 ± 0.04	−8.42 ± 0.03	−137.47 ± 0.00	0.09 ± 0.04	1.09 ± 0.11	0.77 ± 0.05	0.86 ± 0.07
2M18052388-2953056	271.350	−29.885	7.43 ± 0.59	−5.77 ± 0.03	−8.14 ± 0.02	−4.77 ± 0.05	0.09 ± 0.06	1.11 ± 0.26	0.66 ± 0.03	0.85 ± 0.06
2M18065321-2524392	271.722	−25.411	7.91 ± 0.80	−7.64 ± 0.06	−8.61 ± 0.04	−112.08 ± 0.01	0.28 ± 0.14	1.71 ± 0.83	0.60 ± 0.46	0.74 ± 0.13
2M18080306-3125381	272.013	−31.427	10.06 ± 0.73	−1.89 ± 0.05	−4.50 ± 0.04	23.35 ± 0.03	0.13 ± 0.08	2.39 ± 0.80	1.38 ± 0.43	0.89 ± 0.05
2M18104496-2719514	272.687	−27.331	7.30 ± 0.31	−1.79 ± 0.03	−7.09 ± 0.03	−163.54 ± 0.02	0.12 ± 0.05	1.57 ± 0.27	0.63 ± 0.05	0.87 ± 0.05
2M18125718-2732215	273.238	−27.539	8.12 ± 0.34	−5.57 ± 0.02	−7.99 ± 0.02	−86.39 ± 0.00	0.13 ± 0.04	1.14 ± 0.16	0.79 ± 0.09	0.80 ± 0.07
2M18142265-0904155	273.594	−9.071	6.92 ± 0.26	−1.42 ± 0.11	−8.72 ± 0.09	−151.19 ± 0.02	0.28 ± 0.13	3.68 ± 0.28	2.50 ± 0.59	0.87 ± 0.06
2M18143710-2650147	273.655	−26.837	7.46 ± 0.52	−3.66 ± 0.04	−7.43 ± 0.04	−200.72 ± 0.02	0.16 ± 0.13	1.62 ± 0.38	1.07 ± 0.25	0.85 ± 0.14
2M18150516-2708486	273.772	−27.147	6.80 ± 0.38	−0.00 ± 0.03	−9.08 ± 0.02	−141.63 ± 0.02	0.13 ± 0.05	2.28 ± 0.35	1.25 ± 0.22	0.88 ± 0.04
2M18195859-1912513	274.994	−19.214	6.07 ± 0.29	−6.28 ± 0.05	−6.91 ± 0.03	−78.88 ± 0.02	0.10 ± 0.05	2.81 ± 0.24	0.76 ± 0.37	0.93 ± 0.03
2M18200365-3224168	275.015	−32.405	6.27 ± 0.40	−4.20 ± 0.03	−10.36 ± 0.02	−124.55 ± 0.01	0.18 ± 0.08	3.35 ± 0.47	2.19 ± 0.21	0.91 ± 0.05
2M18344461-2415140	278.686	−24.254	7.46 ± 0.50	−3.96 ± 0.03	−8.27 ± 0.02	−171.66 ± 0.02	0.23 ± 0.20	2.63 ± 0.49	2.12 ± 0.12	0.85 ± 0.14
2M18500307-1427291	282.513	−14.458	6.40 ± 0.32	0.13 ± 0.03	−6.71 ± 0.02	−134.03 ± 0.02	0.16 ± 0.07	3.92 ± 0.29	2.49 ± 0.28	0.92 ± 0.03

the StarHorse distances and the proper motions from the *Gaia* EDR3 (Gaia Collaboration et al. 2021). In order to select the best candidate objects that belong to the spheroidal bulge, the following selection criteria were adopted: a maximum distance to the Galactic centre of $d_{GC} < 4$ kpc (Bica et al. 2016); a maximum vertical excursion from the Galactic plane $|z|_{max} < 3.0$ kpc; eccentricity > 0.7; orbits that do not support the bar structure[2] (orbits with frequency ratio $f_R/f_x \neq 2.0 \pm 0.1$; Portail, Wegg & Gerhard 2015); and based on fig. 17 of Queiroz et al. (2021), we selected counter-rotating stars ($V_\phi < 0.0$). Finally, according to the discussion of Section 1, we considered only stars with moderate metallicity of [Fe/H] < -0.80. Applying the selection criteria described above, a sample of 58 stars has been selected. The adopted input parameters for the orbits integration and the orbital parameters are given in Table 1. In Fig. 1, we show the distribution of parameters for our selected stars in comparison with the RPM sample of Queiroz et al. (2021) and our selection is then similar to the metal-poor/high-eccentricity stars discussed in their fig. 20. This figure indicates that our selection is indeed reaching

[2]To estimate this probability, we used the Monte Carlo sample of each star (50 orbits) and calculated the fraction of orbits classified as bar-shaped.

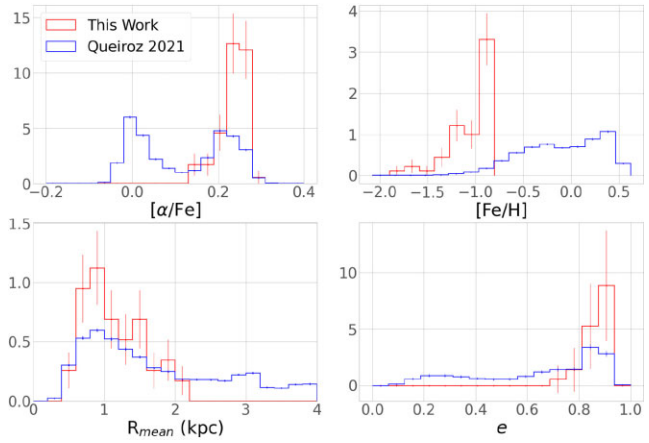

Figure 1. Comparison of the present sample of 58 selected stars (red) and the RPM sample of Queiroz et al. (2021) (blue). Upper panels: normalized distribution of metallicity and alpha-to-iron ratios from APOGEE; lower panels: mean radius $R_{\rm mean} = (R_{\rm apocentre} + R_{\rm pericentre})/2$ and eccentricity of the orbits.

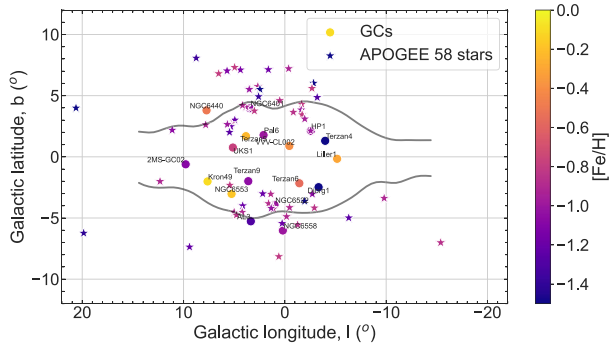

Figure 2. Projected l, b distribution of studied stars in the Galactic bulge region. Symbols: filled stars: this work; filled circles: bulge globular clusters (GCs); solid black line: contours of the bulge. The colours indicate metallicity according to the colour-bar.

bulge stars of the metal-poor spheroid, that are moderately metal-poor, α-rich and in eccentrical orbits but confined to the Galactic centre region. Fig. 2 shows the projected l, b distribution of the sample in the Galactic bulge region.

As explained above, our stars were selected from the reduced-proper-motion sample of Queiroz et al. (2021), and therefore have a signal-to-noise SNR $>$ 50, a good spectral fit from the ASPCAP pipeline ASPCAP_Chi2 $<$ 25, and a radial velocity scatter Vscatter $<$ 1.5 km s^{-1}. As for the renormalized unit weight error – RUWE *Gaia* EDR3 parameter, 56 out of 58 stars in our sample comply with the standard or minimal requirements to get reliable orbital elements, since astrometry from *Gaia* EDR3 has its own caveats. According to the *Gaia* consortium, the RUWE parameter is suggested to return stars astrometrically well-behaved by applying a cut with RUWE $\leq$ 1.4, which is followed by the 56 stars listed in Table 1. The stars 2M17453659-2309130 and 2M18023156-2834451 have a RUWE $>$ 1.4, which makes them sources with astrometric parameters that are not reliable enough.

In Fig. 3, a Kiel diagram of the sample stars is plotted with the effective temperature from ASPCAP and gravity log g coming from the StarHorse output from Queiroz et al. (2020), and compared with the reduced-proper-motion sample of Queiroz et al. (2021).

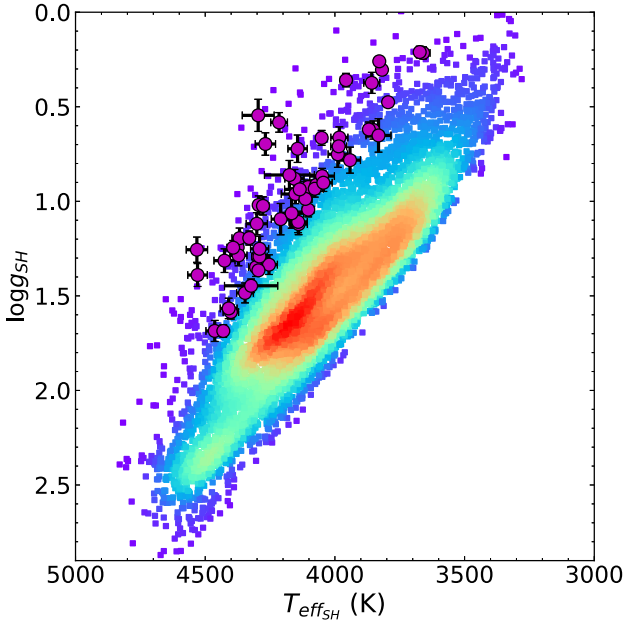

Figure 3. Kiel diagram of the 58 sample bulge stars. (purple circles). In the background, we show the full reduced proper-motion sample of Queiroz et al. (2021).

3 ANALYSIS

We have initially adopted the calibrated stellar parameters effective temperature T$_{\rm eff}$, gravity log g, metallicity [Fe/H], and microturbulence velocity v$_t$ from APOGEE DR16 – we point out that the calibrated parameters give very different element abundances, and should not be used for such aims. In fact, the results from the ASPCAP (García-Pérez et al. 2016) are obtained for the reported non-calibrated spectroscopic stellar parameters. We then adopted these non-calibrated stellar parameterers from DR17, since we became aware that these are obtained from a spectroscopic solution that minimizes the errors in seven dimensions (T$_{\rm eff}$, log g, [Fe/H], v$_t$, [α/Fe], [C/Fe], [N/Fe]).

For this reason, we proceeded with all the rederivation of abundances with the DR17 non-calibrated parameters. These stellar parameters are reported in Table 2, and they are the final parameters adopted.

The abundances were determined by comparing the observed spectra with the synthetic ones. The synthetic spectra calculations are carried out with the code PFANT,[3] as described in Barbuy, Trevisan & de Almeida (2018b). This code is an update of the original FANTOM or ABON2 Meudon code by M. Spite. Each model atmosphere was interpolated in the MARCS grids (Gustafsson et al. 2008).

The atomic line list employed is that from the APOGEE collaboration (Smith et al. 2021). Molecular electronic transition lines of CN $A^2\Pi$–$X^2\Sigma$, vibration-rotation CO $X^1\Sigma^+$, OH $X^2\Pi$, and TiO ϕ-system $b^1\Pi$-$d^1\ \Sigma$ lines were included. The line lists for CN were made available by S. P. Davis, the CO line lists were adopted from Goorvitch (1994), and the OH are from Goldman et al. (1998). For TiO the line list is from Jorgensen (1994). More details on CN, CO, OH, and TiO molecular lines are given in Meléndez & Barbuy (1999), Meléndez, Barbuy & Spite (2001), Meléndez et al. (2003), Schiavon & Barbuy (1999) and Barbuy et al. (2018b).

[3]The code is available at http://trevisanj.github.io/PFANT.

Table 2. Selected 58 stars and corresponding DR17 non-calibrated stellar parameters.

ID	$T_{eff(nc)}$ (K)	log $g_{(nc)}$	[Fe/H]$_{(nc)}$	v_t (kms^{-1})
2M17153858-2759467	3922.7	0.34	−1.62	2.62
2M17173693-2806495	3908.9	0.95	−0.97	2.20
2M17250290-2800385	3796.6	0.91	−0.80	2.39
2M17265563-2813558	4096.2	1.0	−1.31	1.89
2M17281191-2831393	4029.1	0.95	−1.17	1.73
2M17295481-2051262	4205.9	1.50	−0.85	1.71
2M17303581-2354453	3863.0	0.77	−0.99	2.13
2M1732 4257-2301417	3668.2	0.79	−0.82	2.30
2M17330695-2302130	3566.6	0.35	−0.93	2.42
2M17344841-4540171	3869.2	0.85	−0.88	2.16
2M17351981-1948329	3553.5	0.44	−1.11	3.06
2M17354093-1716200	3895.5	1.01	−0.87	2.01
2M17390801-2331379	3740.4	0.83	−0.81	2.34
2M17392719-2310311	3643.3	0.67	−0.87	2.55
2M17473299-2258254	4018.3	0.47	−1.71	2.12
2M17482995-2305299	4213.6	1.24	−1.01	2.10
2M17483633-2242483	3651.5	0.44	−1.09	2.57
2M17503263-3654102	3893.5	0.64	−0.99	2.19
2M17552744-3228019	4018.9	1.0	−1.05	1.99
2M18020063-1814495	3988.8	0.80	−1.38	2.04
2M18050452-3249149	3940.8	0.77	−1.16	2.08
2M18050663-3005419	3439.9	0.23	−0.92	2.52
2M18065321-2524392	3893.1	0.95	−0.89	2.02
2M18104496-2719514	4153.1	1.33	−0.82	2.05
2M18125718-2732215	3617.2	0.44	−1.31	2.64
2M18200365-3224168	3976.6	0.95	−0.86	1.94
2M18500307-1427291	4076.0	1.23	−0.94	1.73
2M17173248-2518529	3977.0	1.0	−0.91	1.81
2M17285088-2855427	3838.0	0.63	−1.20	2.18
2M17291778-2602468	3844.3	0.71	−0.99	2.10
2M17301495-2337002	3814.0	0.69	−1.06	2.22
2M17310874-2956542	4175.7	1.19	−0.92	2.07
2M17382504-2424163	3880.4	0.99	−1.05	1.55
2M17453659-2309130	4133.1	1.27	−1.20	1.08
2M17511568-3249403	3921.2	0.98	−0.90	2.04
2M17532599-2053304	3896.9	0.91	−0.87	2.10
2M17552681-3334272	4051.0	1.08	−0.89	1.98
2M18005152-2916576	4158.9	1.04	−1.02	2.21
2M18010424-3126158	3773.1	0.68	−0.83	2.20
2M18042687-2928348	4164.7	0.88	−1.19	2.14
2M18044663-3132174	3832.6	0.92	−0.90	2.22
2M18052388-2953056	4252.9	0.92	−1.56	1.92
2M18080306-3125381	4310.0	1.57	−0.90	1.48
2M18142265-0904155	3920.5	1.12	−0.85	2.13
2M18195859-1912513	4102.0	1.05	−1.22	1.78
2M17190320-2857321	4139.6	1.19	−1.20	1.83
2M17224443-2343053	4058.3	1.02	−0.88	1.97
2M17292082-2126433	3983.4	0.78	−1.27	2.59
2M17293482-2741164	4143.5	1.03	−1.25	1.85
2M17323787-2023013	3865.7	1.03	−0.85	1.94
2M17330730-2407378	4042.5	0.25	−1.87	1.88
2M17341796-3905103	4163.5	1.42	−0.89	1.84
2M17342067-3902066	4380.4	1.40	−0.90	1.99
2M17503065-2313234	3819.4	0.98	−0.88	2.1
2M18023156-2834451	3617.4	0.42	−1.19	3.02
2M18143710-2650147	4240.5	1.30	−0.91	1.97
2M18150516-2708486	3833.4	1.0	−0.82	2.14
2M18344461-2415140	4294.5	1.09	−1.41	1.83

The atomic lines analysed initially were selected from Smith et al. (2021), Shetrone et al. (2015), Ce II lines identified by Cunha et al. (2017), and lines of S I identified by Fanelli et al. (2021). Lines of Nd II (Hasselquist et al. 2016) and Yb II (Smith et al. 2021) were not studied. In Table 3 are reported the lines that we verified in the spectra of the 58 sample stars.

For the moderately metal-poor sample stars, some of the lines indicated in the articles above are not suitable, and in a few cases we have added other lines that we identified as suitable for the stellar parameters of the sample stars. The lines are discussed in detail below. In the present work, we adopt the ASPCAP abundances of Mg, Si, Ca, and revise the C, N, O, and Ce abundances; we also verified Ti lines and some comments are given, but the abundances are not used, given conflicting results from different lines. Other elements such as Na, Al, and iron-peak elements will be analysed elsewhere.

We identified and fitted the studied lines in the reference stars Arcturus and μ Leo, in order to check if the lines are well reproduced in these stars, and therefore reliable for deriving abundances in the sample stars. For the reference star Arcturus, we used the Hinkle, Wallace & Livingston (1995) atlas, and for the metal-rich reference giant star μ Leo a spectrum from APOGEE was used. The adopted stellar parameters for Arcturus and μ Leo are from Meléndez et al. (2003) and Zoccali et al. (2006) plus Lecureur et al. (2007), respectively.

Table 4 reports abundances in the Sun, Arcturus and μ Leo. For the Sun they are from (a) Grevesse, Noels & Sauval 1996; Grevesse et al. 1998, adopted, (b) Grevesse et al. (2015), Scott et al. (2015a, 2015b), (c) Lodders, Palme & Gail (2009). For Arcturus, the abundances are from Meléndez et al. (2003), Lecureur et al. (2007), Ramírez & Allende Prieto (2011), Barbuy et al. (2014), and Smith et al. (2013). For μ Leo, the abundances are from, Gratton & Sneden (1990), Smith & Ruck (2000), Lecureur et al. (2007), Barbuy et al. (2015), Smith et al. (2013) or present fits, using the observed spectrum by Lecureur et al. (2007) in the optical.

According to Ashok et al. (2021), and Nidever et al. (2015) the average resolution of the APOGEE observations is R $\approx$ 22 500 based on a direct-measured FWHM of ∼0.7 Å, with 10–20 per cent variations seen across the wavelength range. We have employed a typical FWHM = 0.70 Å, but to fit better different lines we varied the FWHM values from 0.60 to 0.75, from the lowest to the highest wavelengths. Note that the FWHM varies from fibers to fibers and with a fiber with wavelength.

3.1 C, N, O abundances

The abundances of C, N, and O are derived from CN, OH, and CO molecular lines. They are interdependent due to the molecular dissociative equilibrium. Since the molecular lines are spread all over the spectra, these abundances are derived first, and they are reported in Table 5.

Computing synthetic spectra employing the PFANT code described in Barbuy et al. (2018b), we have derived C, N, O abundances in two ways:

a) In the region 15144–16896 Å, first we derive the O abundances by analysing the molecular lines of OH. Some of the most prominent OH lines in this region are at: 15264.60, 15266.160, 15278.516, 15281.045, 15719.687, 15893.524, 16074.151, 16662.187, 16872.265, 16895.164 Å. These lines are the most sensitive to oxygen variation in the APOGEE

Table 3. Line list. log gf from VALD3 linelist (Piskunov et al. 1995; Ryabchikova et al. 2015), Kurucz (1993) and NIST (Martin et al. 2002). The log gf values for Ce II lines are from Cunha et al. (2017).

Species	λ (Å)	χ_{ex} (eV)	log gf (VALD3)	log gf (Kurucz)	log gf (NIST)	Notes
Si I	15361.161	5.954	−1.925	−1.990	−1.710	
	15376.831	6.222	−0.649	−0.290	–	
	15833.602	6.222	−0.168	−0.660	−0.078	Apogee gap
	15960.063	5.984	0.107	0.130	0.197	
	16060.009	5.954	−0.566	−0.440	−0.429	
	16094.787	5.964	−0.168	−0.110	−0.078	
	16215.670	5.964	−0.665	−0.990	−0.575	
	16680.770	5.984	−0.140	−0.500	−0.090	
	16828.159	5.984	−1.102	−1.390	−1.012	
Ca I	16197.075	4.535	0.089	0.638	–	
	16204.087	4.535	−0.627	−0.111	–	
Ti I	15543.756	1.879	−1.120	−1.273	−1.080	
	15602.842	2.267	−1.643	−1.544	–	
	15698.979	1.887	−2.060	−2.218	−2.020	
	15715.573	1.873	−1.250	−1.359	−1.200	
	16635.161	2.345	−1.807	−2.178	–	
Ce II	15277.610	0.609	−1.94	–	–	too faint
	15784.750	0.318	−1.54	–	–	
	15829.830	0.320	−1.80	–	–	Apogee gap
	15958.400	0.470	−1.71	–	–	
	15977.120	0.232	−2.10	–	–	weak line strongly blended
	16327.320	0.561	−2.40	–	–	
	16376.480	0.122	−1.79	–	–	
	16595.180	0.122	−2.19	–	–	
	16722.510	0.470	−1.65	–	–	

Table 4. Solar abundances from (1) Grevesse et al. (1996), Grevesse & Sauval (1998) (adopted); (2) Steffen et al. (2015); (3) Scott et al. (2015a, 2015b); (4) Grevesse et al. (2015); (5) Lodders et al. (2009); Arcturus abundances from: (6) Ramírez & Allende Prieto (2011), (7) McWilliam et al. (2013), (8) Lecureur et al. (2007), (9) Barbuy et al. (2014), (10) Smith et al. (2013); (11) Cunha et al. (2017) μ Leo abundances from: (10) Smith et al. (2013); (12) Gratton & Sneden (1990), 13: Barbuy et al. (2015), (14) Van der Swaelmen et al. (2016). The last column lists values from Smith et al. (2013).

El.	Z	$\log \epsilon(X)_\odot$ Sun			[X/Fe]	$\log \epsilon(X)$ Arcturus adopted	[X/Fe]	$\log \epsilon(X)$ μ Leo adopted	
Fe	26	7.50	7.50	7.50	−0.54	6.96	+0.30	7.80	7.76[10]
C	6	8.55[1]	–	8.39[5]	−0.22[8]	7.79	−0.3[10]	8.55	8.52[10]
N	7	7.97[1]	–	7.86[5]	+0.22[8]	7.65	+0.45[10]	8.72	8.71[10]
O	8	8.76[2]	–	8.73[5]	0.39[9]	8.62	+0.0[10]	9.06	9.05[10]
Na	11	6.33[1]	6.21[3]	6.30[5]	0.11[6]	5.90	+0.50[8]	7.13	–
Mg	12	7.58[1]	7.59[3]	7.54[5]	0.37[6]	7.41	−0.03[10]	7.85	7.85[10]
Al	13	6.47[1]	6.43[3]	6.47[5]	0.37[7]	6.30	+0.13[10]	6.90	6.90[10]
Si	14	7.55[1]	7.51[3]	7.52[5]	0.33[6]	7.34	−0.10[10]	7.75	7.76[10]
Ca	20	6.36[1]	6.32[3]	6.33[5]	0.11[6]	5.93	−0.04[10]	6.62	6.62[10]
Sc	21	3.17[1]	3.16[3]	3.10[5]	0.23[6]	2.86	+0.10[11]	3.57	–
Ti	22	5.02[1]	4.93[3]	4.90[5]	0.26[7]	4.74	+0.10[10]	5.42	5.40[10]
V	23	4.00[1]	3.89[3]	4.00[5]	0.12[7]	3.58	+0.03[12]	4.33	4.18[10]
Cr	24	5.67[1]	5.62[3]	5.64[5]	−0.05[6]	5.08	−0.01[12]	5.96	6.14[10]
Mn	25	5.39[1]	5.42[3]	5.37[5]	−0.14[7]	4.71	+0.00[12]	5.69	5.79[10]
Co	27	4.92[1]	4.93[3]	4.92[5]	+0.09[7]	4.49	+0.00[12]	5.22	5.23[10]
Ni	28	6.25[1]	6.20[3]	6.23[5]	0.06[6]	5.77	+0.05[10]	6.60	6.60[10]
Cu	29	4.21[1]	4.19[4]	4.21[5]	−0.26[10]	3.55	−0.10[10]	4.41	4.41[10]
Zn	30	4.60[1]	4.56[4]	4.62[5]	+0.18[6]	4.26	−0.10[13]	4.80	–
Y	39	2.24[1]	2.21[4]	2.21[5]	−0.30[9]	1.40	+0.04[14]	2.58	–
Zr	40	2.60[1]	2.59[4]	2.58[5]	−0.28[7]	1.78	+0.10[12]	3.00	–
Ba	56	2.13[1]	2.25[4]	2.17[5]	−0.30[9]	1.29	+0.10[14]	2.53	–
La	57	1.22[1]	1.11[4]	1.14[5]	−0.30[9]	0.38	−0.37[14]	1.15	–
Ce	58	1.55[1]	1.58[4]	1.61[5]	−0.45[11]	0.99	−0.37[14]	1.15	–
Eu	63	0.51[1]	0.52[4]	0.52[5]	0.23[7]	0.20	−0.14[14]	0.67	–

Table 5. Revised CNO abundances derived from non-calibrated DR17 stellar parameters compared with the DR17 CNO abundances in the last column.

ID	[C/Fe]	[N/Fe]	[O/Fe]	[C/Fe]	[N/Fe]	[O/Fe]
	present work			DR17		
b1 2M17153858-2759467	−0.60	0.40	0.35	−0.57	0.33	0.19
b2 2M17173693-2806495	−0.20	0.00	0.40	−0.07	0.15	0.33
b3 2M17250290-2800385	−0.05	0.10	0.35	0.09	0.15	0.32
b4 2M17265563-2813558	−0.35	0.20	0.35	−0.29	0.29	0.30
b5 2M17281191-2831393	−0.30	0.40	0.40	−0.18	0.23	0.30
b6 2M17295481-2051262	−0.30	0.20	0.40	−0.07	0.04	0.35
b7 2M17303581-2354453	−0.25	0.00	0.40	−0.06	0.17	0.35
b8 2M17324257-2301417	+0.00	−0.10	0.35	0.11	0.11	0.33
b9 2M17330695-2302130	0.00	0.00	0.35	0.18	−0.02	0.30
b10 2M17344841-4540171	−0.30	0.20	0.35	−0.11	0.17	0.35
b11 2M17351981-1948329	−0.10	0.10	0.40	0.00	0.04	0.17
b12 2M17354093-1716200	−0.20	0.00	0.37	−0.03	0.13	0.32
b13 2M17390801-2331379	−0.10	0.15	0.38	0.05	0.19	0.31
b14 2M17392719-2310311	−0.10	0.10	0.38	0.02	0.18	0.26
b15 2M17473299-2258254	−0.70	0.80	0.35	−0.49	0.45	0.29
b16 2M17482995-2305299	−0.30	0.30	0.40	−0.43	0.54	0.34
b17 2M17483633-2242483	−0.20	0.10	0.35	−0.08	0.10	0.19
b18 2M17503263-3654102	−0.40	0.40	0.33	−0.17	0.22	0.33
b19 2M17552744-3228019	−0.30	0.40	0.35	−0.18	0.20	0.32
b20 2M18020063-1814495	−0.50	0.30	0.35	−0.42	0.24	0.24
b21 2M18050452-3249149	−0.50	0.20	0.40	−0.29	0.26	0.32
b22 2M18050663-3005419	−0.10	0.00	0.40	0.01	0.02	0.17
b23 2M18065321-2524392	−0.20	0.20	0.38	−0.04	0.14	0.33
b24 2M18104496-2719514	−0.10	0.10	0.35	−0.03	0.21	0.33
b25 2M18125718-2732215	−0.22	0.20	0.40	−0.16	0.15	0.11
b26 2M18200365-3224168	−0.35	0.20	0.32	−0.15	0.25	0.33
b27 2M18500307-1427291	−0.30	0.20	0.38	−0.14	0.10	0.32
c1 2M17173248-2518529	−0.25	0.20	0.38	−0.17	0.12	0.21
c2 2M17285088-2855427	−0.45	0.40	0.40	−0.28	0.16	0.28
c15 2M17291778-2602468	−0.20	0.30	0.38	−0.08	0.16	0.31
c3 2M17301495-2337002	−0.25	0.20	0.40	−0.12	0.22	0.27
c16 2M17310874-2956542	−0.40	0.20	0.36	−0.14	0.22	0.36
c17 2M17382504-2424163	−0.20	0.30	0.40	−0.06	0.16	0.25
c4 2M17453659-2309130	−0.30	0.30	0.40	−0.24	0.06	0.25
c18 2M17511568-3249403	−0.20	0.00	0.38	−0.04	0.16	0.34
c5 2M17532599-2053304	−0.25	0.20	0.40	−0.04	0.21	0.31
c19 2M17552681-3334272	−0.30	0.00	0.40	−0.16	0.17	0.35
c20 2M18005152-2916576	−0.40	0.20	0.40	−0.20	0.30	0.33
c21 2M18010424-3126158	−0.25	0.00	0.38	−0.09	0.18	0.28
c22 2M18042687-2928348	−0.50	0.30	0.40	−0.34	0.29	0.31
c6 2M18044663-3132174	−0.15	0.00	0.40	0.02	0.14	0.31
c23 2M18052388-2953056	−0.35	0.40	0.40	−0.45	0.34	0.38
c7 2M18080306-3125381	−0.30	0.00	0.40	−0.09	0.05	0.40
c24 2M18142265-0904155	−0.20	0.20	0.33	0.02	0.17	0.33
c8 2M18195859-1912513	−0.40	0.40	0.40	−0.28	0.15	0.30
c9 2M17190320-2857321	−0.30	0.20	0.70	−0.24	0.19	0.33
c10 2M17224443-2343053	−0.35	0.20	0.37	−0.11	0.38	0.34
c11 2M17292082-2126433	−0.60	0.60	0.38	−0.54	1.06	0.22
c25 2M17293482-2741164	−0.50	0.30	0.40	−0.33	0.32	0.34
c12 2M17323787-2023013	−0.15	0.20	0.40	0.04	0.13	0.33
c13 2M17330730-2407378	−0.70	0.70	0.38	−0.73	0.30	0.30
c26 2M17341796-3905103	−0.40	0.25	0.40	−0.07	0.20	0.34
c27 2M17342067-3902066	−0.30	0.20	0.40	−0.14	0.29	0.45
c28 2M17503065-2313234	−0.10	0.00	0.35	0.08	0.16	0.33
c14 2M18023156-2834451	−0.05	0.10	0.40	0.01	0.07	0.18
c29 2M18143710-2650147	−0.30	0.10	0.40	−0.14	0.27	0.34
c30 2M18150516-2708486	−0.05	0.00	0.31	0.08	0.14	0.32
c31 2M18344461-2415140	−0.45	0.40	0.40	−0.39	0.25	0.37

Table 6. Abundances from original ASPCAP derivations, and revised values of Ce, using the lines reported in Table 3 for the 58 sample stars. For Ce abundances the two columns correspond to DR17 ASPCAP abundances, and revised values.

Star ID	[Ce/Fe] DR17	[Ce/Fe] revised
2M17153858-2759467	−0.16	0.25
2M17173693-2806495	−0.10	0.20
2M17250290-2800385	–	0.20
2M17265563-2813558	−0.20	0.10
2M17281191-2831393	−0.14	0.20
2M17295481-2051262	−0.02	−0.02
2M17303581-2354453	–	0.40
2M17324257-2301417	–	–
2M17330695-2302130	–	0.50
2M17344841-4540171	–	0.50
2M17351981-1948329	–	0.50
2M17354093-1716200	–	0.50
2M17390801-2331379	–	0.50
2M17392719-2310311	–	0.50
2M17473299-2258254	−0.27	0.30
2M17482995-2305299	−0.4	0.20
2M17483633-2242483	–	0.50
2M17503263-3654102	–	0.50
2M17552744-3228019	−0.15	0.35
2M18020063-1814495	−0.08	0.30
2M18050452-3249149	−0.11	0.45
2M18050663-3005419	–	0.40
2M18065321-2524392	–	0.45
2M18104496-2719514	−0.17	0.25
2M18125718-2732215	–	0.30
2M18200365-3224168	0.07	0.50
2M18500307-1427291	0.08	0.45
2M17173248-2518529	0.03	0.45
2M17285088-2855427	–	0.50
2M17291778-2602468	–	0.45
2M17301495-2337002	–	0.45
2M17310874-2956542	−0.17	0.30
2M17382504-2424163	–	0.10
2M17453659-2309130	−0.40	−0.10
2M17511568-3249403	−0.11	0.40
2M17532599-2053304	–	0.40
2M17552681-3334272	0.03	0.35
2M18005152-2916576	−0.12	0.30
2M18010424-3126158	–	0.43
2M18042687-2928348	−0.07	0.20
2M18044663-3132174	–	0.33
2M18052388-2953056	−0.29	0.20
2M18080306-3125381	0.15	0.25
2M18142265-0904155	−0.15	0.30
2M18195859-1912513	−0.17	0.35
2M17190320-2857321	−0.20	0.32
2M17224443-2343053	0.13	0.55
2M17292082-2126433	−0.12	0.42
2M17293482-2741164	−0.27	0.30
2M17323787-2023013	–	0.42
2M17330730-2407378	−0.18	0.30
2M17341796-3905103	−0.03	0.20
2M17342067-3902066	−0.18	0.20
2M17503065-2313234	–	0.20
2M18023156-2834451	–	0.50
2M18143710-2650147	−0.18	0.20
2M18150516-2708486	–	0.25
2M18344461-2415140	−0.28	0.40

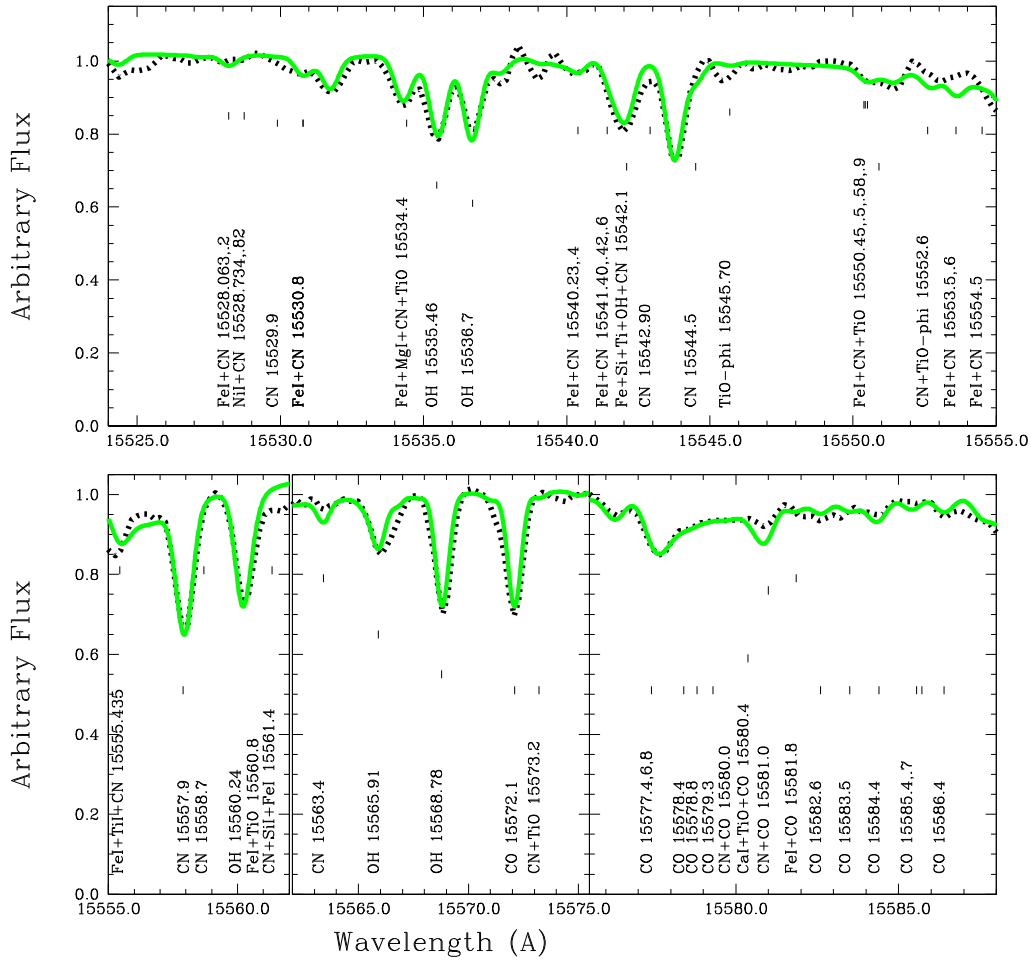

Figure 4. Star 2M17382504-2424163: Observed spectrum (black dotted) and synthetic spectrum computed with [C, N, O/Fe] = −0.20, 0.30, 0.40 (green).

sample. We derive C abundances by analysing the CO molecular lines, but there are not many strong CO lines in the range of 15100–17000 Å. In our sample, the strongest lines of CO, used to measure C abundances, are at 15983.214, 15985.598, 15990.420, 16016.081 Å. Next we see how the CN lines change when we modify Nitrogen. The most sensitive lines of CN are at 15162.648, 15222.382 Å. There are many CN lines in the region we are working with (especially in the range 15522–15600 Å), but most of them are too shallow to give reliable abundance measurements.

b) A derivation of CNO abundances using the region 15525–15595 Å, where there are clear lines of OH, and a clear bandhead of CO, as well as lines of CN, although less conspicuous, as done for example in Barbuy et al. (2021a) for Phoenix spectra that were observed in this region only. For these calculations a FWHM = 0.60 was adopted which is suitable for the wavelength region in question.

This is illustrated in Fig. 4 for star 2M17382504-2424163. Note the clear OH lines at 15535.46, 15565.91, 15566.78, and clear CO bandhead at 15577.4 Å.

We concluded that both methods a) and b) give very similar results within ±0.1 dex.

A verification of these CNO abundances was carried out by fitting lines along all the spectra, in particular the lines of CO 15600.74, 15612.5, 15667.55 Å, where only for four stars the C abundance was decreased by −0.05 to −0.10 (stars 2M17330695-2302130, 2M18050663-3005419, 2M18125718-2732215, and 2M18344461-2415140), and for the others the fits were very satisfactory.

We then proceeded with the verification of the OH lines: OH 15130.921, 15266.168, 15281.052, 15409.172, 15568.78, 15651.896, 15719.696, 15755.522 Å, and CN 5181.277, 15298.487, 15308.893, 15318.74, 15337.959, 15341.508, 15432.811, 15447.095, 15466.235, 15481.868, 15530.776, 15684.088, 15737.445 Å. Only for star 2M18023156-2834451 we increased the oxygen abundance by 0.05 dex, noting that its spectra show larger lines than the others, needing a higher spectral convolution to be fitted.

Fits are shown for selected OH lines for star 2M17382504-2424163 in Fig. 5, and CO lines in Fig. 6 for stars 2M17382504-2424163 and 2M17511568-3249403.

Regions of CN lines are verified using wavelength regions indicated by Fernández-Trincado et al. (2020a, 2020b) for example. Fig. 7 are shown the fits to good CN lines. Among these, the clearest CN feature is at 15387.6 Å, and its fits are compatible with the C, N abundances from the 15283–15287, 15320–15330, and 15355–15380 Å regions. The feature at 15514 Å is blended with a Co I line and is less reliable. The N abundances derived are confirmed for about half the stars, whereas for the other half the N abundance was decreased by a mean of 0.2 dex: this is not surprising because the CN lines in the 15555 ± 50 Å from method b) are all faint and/or blended. Results from method b) above, together with these corrections, are adopted for C, N, O abundances.

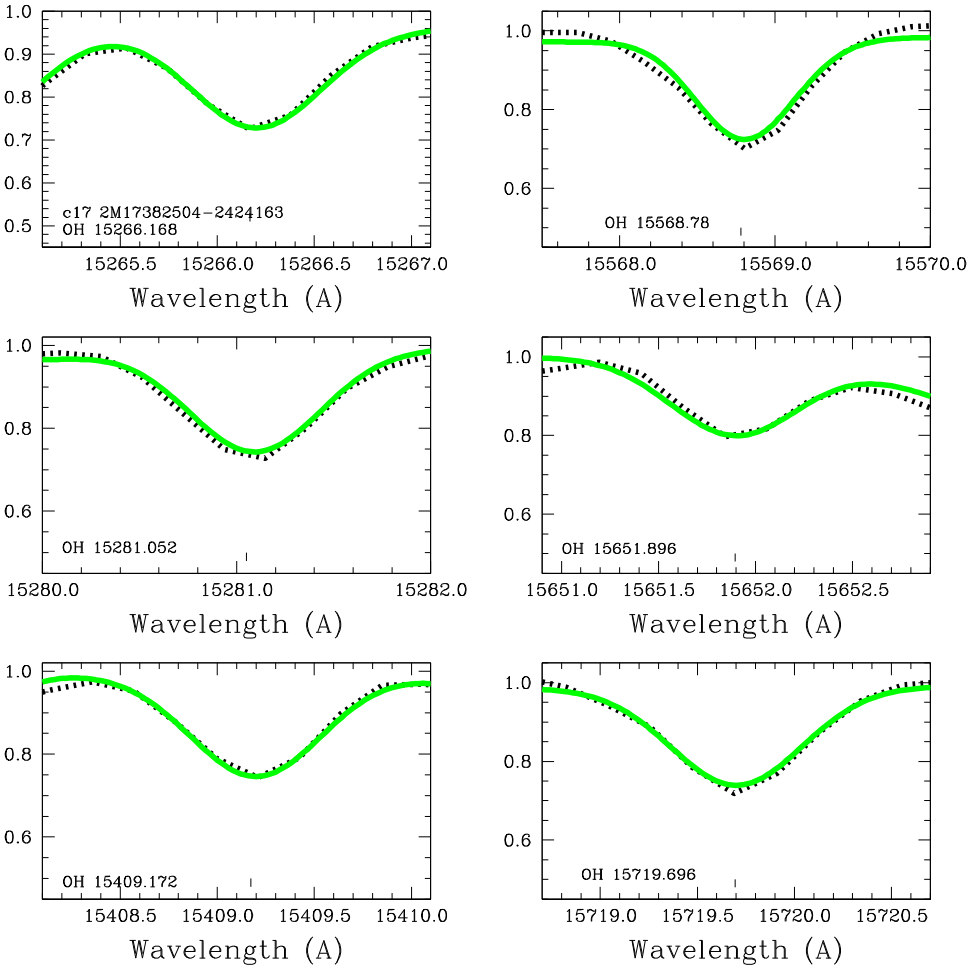

Figure 5. Star 2M17382504-2424163: Selected OH lines. Observed spectrum (black dotted) and synthetic spectrum computed with [O/Fe] = 0.40 (green).

The results of our manual analysis differ from the outputs of the ASPCAP pipeline for oxygen and, to a lesser degree nitrogen. Our methods a) and b) give rather similar results to each other within ±0.05 dex, and with oxygen abundances somewhat higher than those derived with ASPCAP that appear to be too low for bulge stars. The uncertainties on the oxygen abundances were already discussed by Jönsson, Allende Prieto & Holtzman (2018), and Zasowski et al. (2019). Our oxygen abundances as compared with the DR17 ones are compatible within uncertainties, but with a trend to be higher.

In order to verify the reason for these differences, we carried out the fit to the N-rich star 2M17480576-2445000 analysed by Schiavon et al. (2017). With our method b) we have found that [O/Fe] = 0.4 instead of [O/Fe] = 0.3, and [C/Fe] = −0.2 instead of [C/Fe] = 0.0, and on the other hand the N enhancement of [N/Fe] = 0.8 is confirmed. Given the interplay between the CNO trio elements, it appears that the trend is to have somewhat lower C and higher O, and not much of a change in N abundances, in comparing our abundances with those from ASPCAP.

Note that none of the stars in our sample is N-enhanced, therefore they are good candidates to being similar to the first generation stars found in globular clustes.

3.2 alpha-elements Mg, Si, Ca, and Ti

We analyse the abundances of the α-elements Mg, Si, and Ca, and the iron-peak element Ti.

3.2.1 Magnesium, Silicon, Calcium and Titanium

Our fits with the original DR17 ASPCAP Mg abundances are in agreement with their results for Mg, Si, and Ca. Our calculations are in LTE with plane-parallel models, as is adopted by the original ASPCAP method. The DR17 results for Mg and Ca correspond to calculations in non-LTE (Osorio et al. 2020), and even so the compatibility is good for these elements.

The Si I lines reported in Table 3 are all suitably reproduced with the ASPCAP Si abundance with the exception of line Si I 15261.161 that is too shallow in the sample stars. Si abundance appears to be among the best determined ones by ASPCAP together with Mg.

The four Ca I lines listed in Smith et al. (2013) and that are used to ASPCAP, namely 16136.8, 16150.8, 16155.2, 16157.4 Å (see also Jönsson et al. 2018) are faint in the sample stars, and they are not fitted with the ASPCAP Ca abundance; instead they would need an extra 0.2 dex in Ca abundance to be fitted. In Table 3, we include another two lines of Ca I that we were able to identify as suitable for the metallicity of our stars: Ca I 16197.075, 16204.087 Å. The Ca I 16197.075 is well fitted in about half the stars, whereas in others it show blends, and finally the Ca I 16204.087 Å line is well fitted with the Ca abundance from ASPCAP. A FWHM = 0.65 fits better the lines. In conclusion, we adopted the ASPCAP Ca abundances, relying on the results for the Ca I 16204.087 Å line.

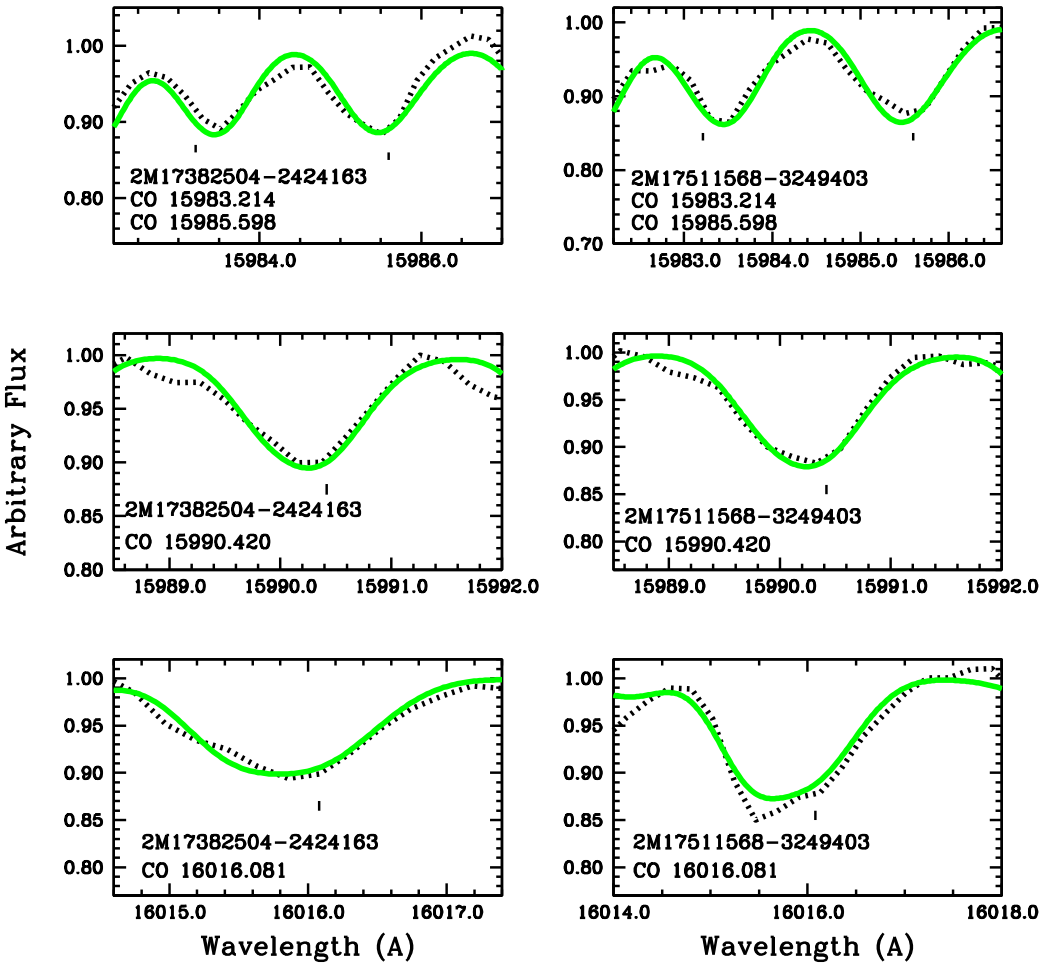

Figure 6. Stars 2M17382504-2424163 and 2M17511568-3249403: Selected CO lines. Observed spectra (black dotted) and synthetic spectra computed with [C/Fe] = −0.2 for both stars, and [O/Fe] = 0.40 and 0.38, respectively (green).

3.2.2 Titanium

Among the five lines studied, only Ti I 15543.756 Å line is well fit in essentially all stars. Ti I 15698.979 Å tends to give the same value, but it is located in a blend with several other lines with a difficult continuum placement. Ti I 15715.753 Å tends to give either the value from ASPCAP or requires a lower Ti abundance, whereas Ti I 15602.842 and 16635.161 Å require higher values by about 0.3 ± 0.2 dex to be fitted. Because of the conflicting results from these different lines, and the fact that ASPCAP gives [Ti/Fe] = 0.0 for most stars, which is not compatible with the Si and Ca enhancements, we preferred not to analyse the Ti abundances in the sample stars.

Note that the lines Ti I 15602.842 and 16635.161 Å, that are only fitted with higher Ti abundances, have somewhat higher excitation potential than the other three inspected lines, and that means that there may be an effect of effective temperature.

3.3 s-process element Ce

We used six Ce II lines, among which Ce II 16722.510 Å line is well fit to almost all stars except for a few for which most of the other lines are fit with a lower value than with the best line (case of 2M17173693-2806495), followed by Ce II 15958.400 and 16595.180 Å lines, that are fit with the adopted value for almost all stars. The Ce abundances from APOGEE DR17 and revised values are given in Table 6.

Ce II 15784.750 Å is fit for about half the stars, for a few would require lower Ce abundances and about 1/3 of them would require higher Ce abundances; 16327.320 Å is faint and is fit for about 1/3 of stars and 2/3 would require higher Ce abundances; Ce II 16376.480 Å would require higher values for about half the stars.

In eight cases all six lines can be considered well-fitted, as is the case of star 2M18500307-1427291, shown in Fig. 8.

For the fit of the Ce lines, we adopted FWHM = 0.75, which is suitable for the wavelength of the lines. The revised values are systematically higher than those resulting from ASPCAP (the fits to all stars are available under request).

DR17 used three Ce II windows covering the lines 15784, 16376, and 16595 Å. These are the stronger lines among the six that we used, and for all the sample stars it is clear that, from these three lines, a higher Ce abundance is needed.

We note that due to uncertainties in the Ce abundances in DR17 the APOGEE team has released internally to the collaboration a value added catalogue with revised abundances (Hayes et al. in preparation). This catalogue will be public to the community in a few months.

As for Nd, we found that the lines are not suitable for analysis, from fits to them in the reference stars Arcturus and μ Leo, therefore we disregarded this element in the present analysis.

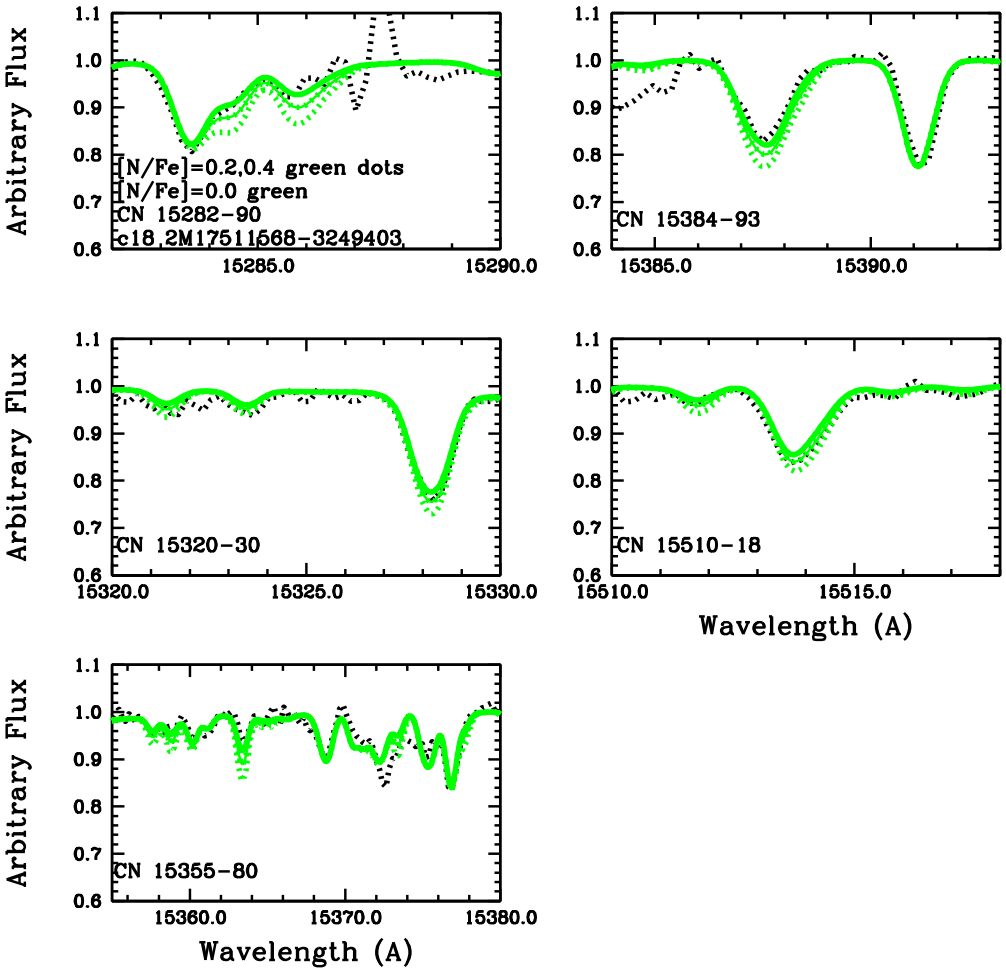

Figure 7. Star 2M17511568-3249403: regions containing CN lines. Observed spectra (black dotted) and synthetic spectra (green) computed with [C/Fe] = −0.2, [N/Fe] = 0.0, [O/Fe] = 0.38; green dotted lines correspond to calculations with [N/Fe] = 0.2, 0.4.

4 DISCUSSION

The α-element abundances in bulge stars provide us with a constraint on the formation history of its stellar populations: the formation timescale. In other words, a mean [α/Fe] $\sim$ 0.5 in halo and bulge metal-poor stars of [Fe/H] $\lesssim -1.0$ indicates a fast chemical enrichment at early times, dominated by supernovae type II (SN II) (e.g. Woosley & Weaver 1995, hereafter WW95), whereas a lower [α/Fe] implies a slower enrichment, allowing supernovae type Ia to contribute to the enrichment of iron.

Moreover, as recently shown by Miglio et al. (2021) for a sample of Kepler stars with APOGEE spectra, stars with [α/Fe] > 0.2 are all very old. The same probably applies to the present sample.

4.1 Oxygen and magnesium

Oxygen is produced by helium and neon burning in hydrostatic phases of the evolution of massive stars. Magnesium, together with Aluminum, are produced in hydrostatic carbon and neon burning (WW95). O and Mg are therefore the bona-fide alpha-elements produced by massive stars and ejected by supernova type II (SN II) event. They are enhanced relative to iron in old stellar populations, such as in bulge stars. In Fig. 9, upper panel are plotted the oxygen abundances reported by the original APOGEE DR17 release, and the revised values obtained as explained in Section 3. This Figure is readapted from that in Barbuy et al. (2018a), taking into account only the literature higher-resolution data (with a few exceptions) and data showing little abundance spread. The literature data taken into account are from Friaça & Barbuy (2017), that contains a revision of the abundances from Zoccali et al. (2006) and Lecureur et al. (2007), Cunha & Smith (2006); Alves-Brito et al. (2010), Fulbright, McWilliam & Rich (2007), only stars older than 11 Gyr from Bensby et al. (2013), Ryde et al. (2010) including a few of the same stars from Zoccali et al. (2006), Jönsson et al. (2017) including reanalysed 23 stars from Zoccali et al. (2006), Lecureur et al. (2007) and Friaça & Barbuy (2017), Siqueira-Mello et al. (2016), and metal-poor stars from García-Pérez et al. (2013), Howes et al. (2016) and Lamb et al. (2017).

Fig. 9 (lower panel) gives [Mg/Fe] versus [Fe/H] for metal-poor stars from García-Pérez et al. (2013), Howes et al. (2016), Lamb et al. (2017), Casey & Schlaufman (2015), Koch et al. (2016), Fulbright et al. (2007), as corrected by McWilliam (2016), Alves-Brito et al. (2010), Hill et al. (2011), Bensby et al. (2017) for stars older than 8 Gyr, Johnson et al. (2014), Ryde et al. (2010, 2016), Siqueira-Mello et al. (2016), Jönsson et al. (2017) and Rojas-Arriagada et al. (2017).

Our fits show agreemeent with the ASPCAP Mg abundances, and they are compatible with the Mg abundances of other samples of bulge stars. The different model lines in Fig. 9 correspond to different radii from the Galactic centre.

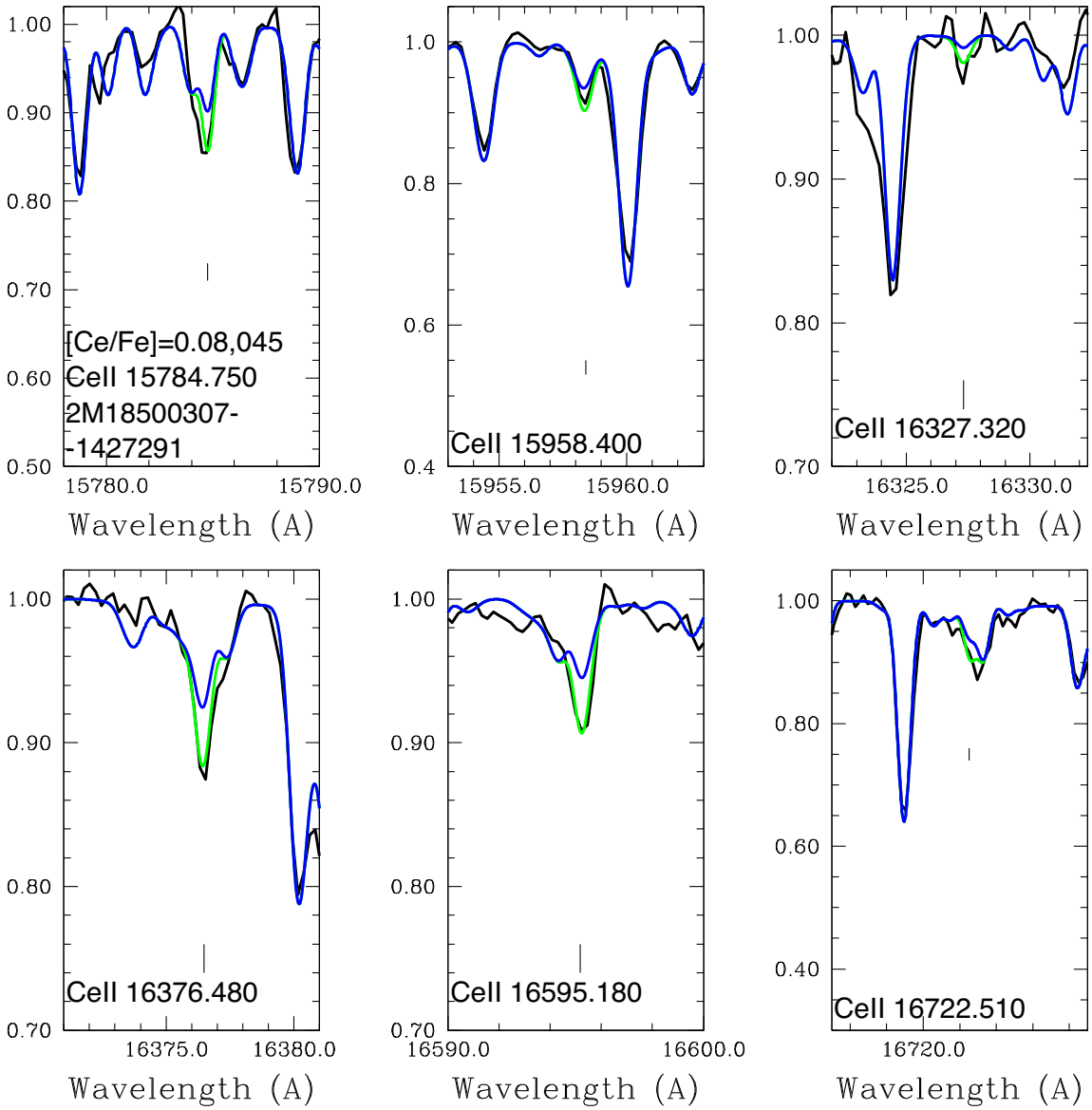

Figure 8. Star 2M18500307-1427291: fit to the six cerium lines. Observed spectrum: black; synthetic spectra are: blue with original ASPCAP [Ce/Fe] = 0.08 Ce abundance, green with final Ce abundance.

4.2 Chemodynamical evolution model for O and Mg

We have compared the abundances derived from observations with the predictions of chemodynamical evolution models for the bulge (Friaça & Barbuy 2017), described as a classical spheroid. It is assumed a baryonic mass of $2 \times 10^9\,M_\odot$, and a dark halo mass $M_H = 1.3 \times 10^{10}\,M_\odot$. One central parameter of the model is the specific star formation rate ν_{SF} (i.e. the inverse of the star formation time-scale).

In the nucleosynthesis prescriptions of our model, we adopt the metallicity dependent yields from core-collapse supernovae (SNe II) from WW95 with some modifications following suggestions of Timmes, Woosley & Weaver (1995). For low metallicities ($Z < 0.01\,Z_\odot$), we included the yields from high explosion-energy hypernovae (HNe) (Nomoto et al. 2013, and references therein). The type Ia supernovae yields are from Iwamoto et al. (1999) – their models W7 (progenitor star of initial metallicity $Z = Z_\odot$) and W70 (zero initial metallicity). The yields for intermediate mass stars (0.8–8 $M_\odot$) with initial Z = 0.001, 0.004, 0.008, 0.02, and 0.4 come from van den Hoek & Groenewegen (1997) (variable η_{AGB} case).

As we can see from Fig. 9, the abundances derived here both for the oxygen (upper panel) and for the magnesium (lower panel) are well reproduced by the chemodynamical model with $\nu_{SF} = 1\,Gyr^{-1}$ (star formation time-scale of 1 Gyr). Once more this suggests these objects to be very old.

4.3 Silicon and calcium

Si and Ca are mainly produced during the explosive nucleosynthesis of SN II events (WW95; McWilliam 2016) with smaller contributions from supernovae type Ia (SNIa).

The α-elements Si and Ca are plotted in Fig. 10 for the 58 sample stars together with literature data from García-Pérez et al. (2013), Howes et al. (2016), Lamb et al. (2017), Casey & Schlaufman (2015), Koch et al. (2016), Alves-Brito et al. (2010), Bensby et al. (2017) for

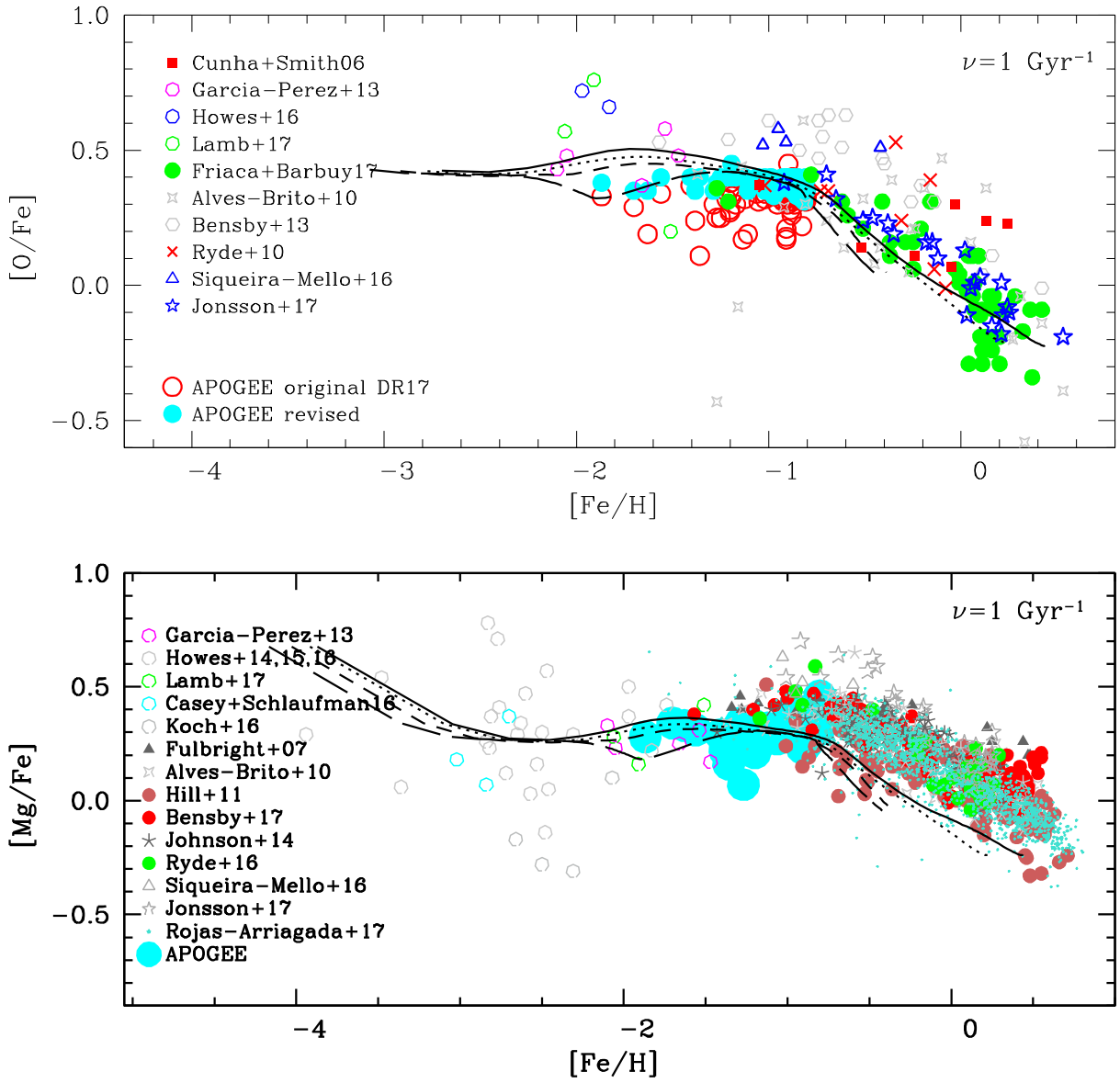

Figure 9. [O/Fe] versus [Fe/H] (upper panel) and [Mg/Fe] versus [Fe/H] (lower panel), for literature bulge field stars and the APOGEE abundances (original and revised in the case of oxygen) for the 58 sample stars. Symbols: grey 4-pointed stars: Alves-Brito et al. (2010); red filled circles: Bensby et al. (2013); red filled circles: Bensby et al. (2017); grey open pentagons: Casey & Schlaufman (2015); strong-grey filled triangles: Fulbright et al. (2007); magenta open pentagons: García-Pérez et al. (2013); red filled squares: Cunha & Smith (2006); indianred filled circles: Hill et al. (2011); grey open pentagons: Howes et al. (2016); grey stars: Johnson et al. (2014); grey 5-pointed stars: Jönsson et al. (2017); grey open pentagons: Koch et al. (2016); green open pentagons: Lamb et al. (2017); red crosses: Ryde et al. (2010); green filled circles: Ryde et al. (2016); turquoise 5-pointed stars: Rojas-Arriagada et al. (2017); grey open triangles: Siqueira-Mello et al. (2016); blue open circles: APOGEE original; cyan filled circles: final abundances for the 58 APOGEE sample stars. The oxygen abundances are normalized in terms of adopted solar abundances as explained in Friaça & Barbuy (2017). Chemodynamical evolution models from Friaça & Barbuy (2017) with formation time-scale of 1 Gyr, for several radii, are overplotted: $r < 0.5$ kpc (solid lines), $0.5 < 1$ kpc (dotted lines), $1 < r < 2$ kpc (short-dashed lines), $2 < r < 3$ kpc (long-dashed lines).

stars older than 8 Gyr, Ryde et al. (2016) and Siqueira-Mello et al. (2016).

Fig. 10 shows that a typical star formation time-scale of 1 Gyr (the chemodynamical model with $\nu_{SF} = 1\,\mathrm{Gyr}^{-1}$) also explains the Si and Ca abundances found in the bulge.

From this figure, we can conclude that there are no differences in the Si and Ca abundances of the present confirmed *in situ* samples of bulge stars, and previous samples in bulge regions, for which no precise distances were available.

4.4 Heavy element Ce

In Fig. 11 are shown the revised Ce abundances in contrast with the lower original DR17 APOGEE abundances, together with results for M62 from Yong et al. (2014) and for field bulge stars from van der Swaelmen et al. (2016) and Lucey et al. (2022). As can be seen from the figure, we have found that the sample stars are enhanced in Cerium by about a mean value of [Ce/Fe] $\sim$ 0.4. We find Ce enhancements relative to the DR17 and as well to results from the

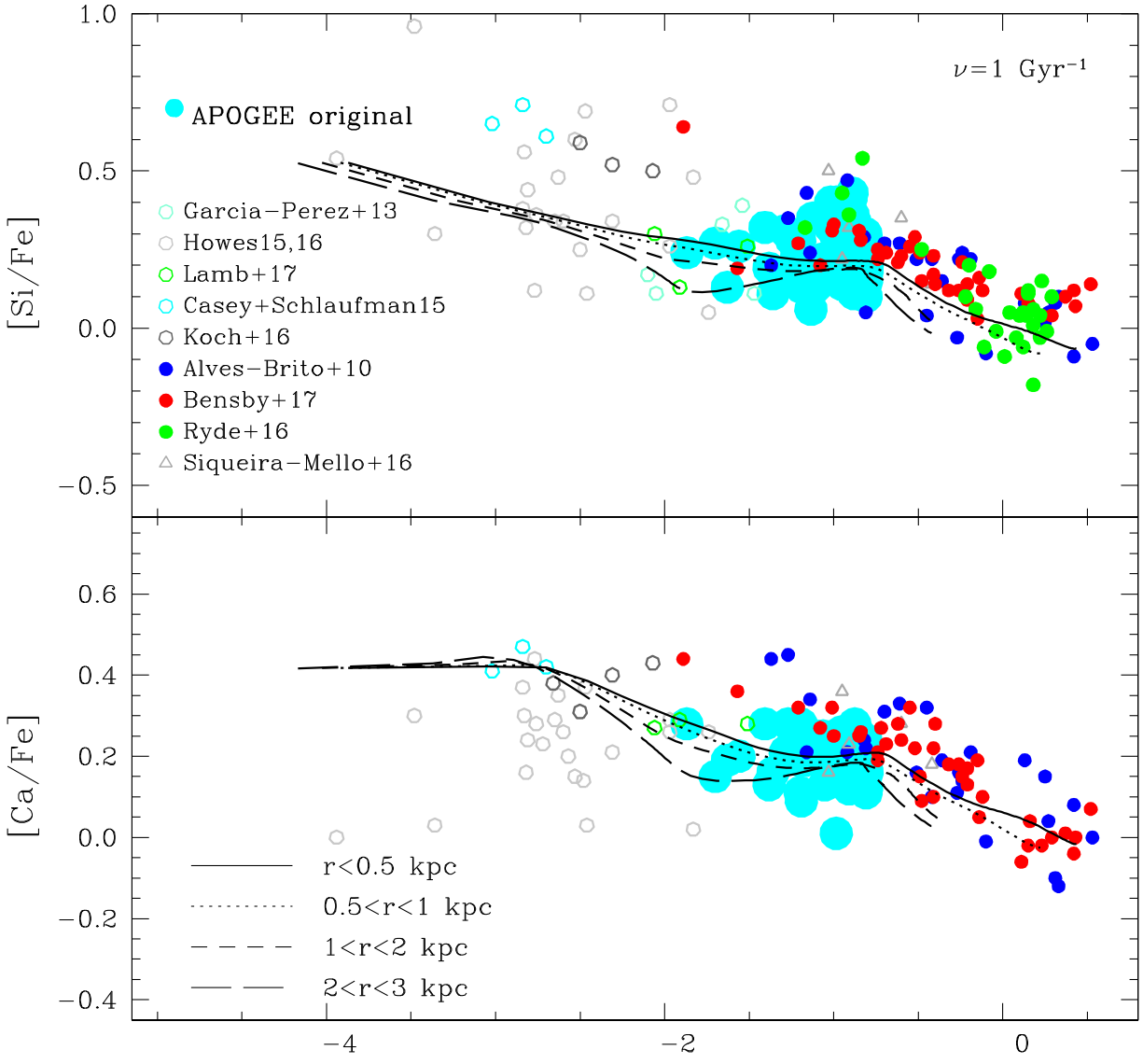

Figure 10. [Si, Ca/Fe] versus [Fe/H] for literature bulge field stars and the APOGEE abundances for the 58 sample stars. Symbols: grey 4-pointed stars: Alves-Brito et al. (2010); red filled circles: Bensby et al. (2017); grey open pentagons: Casey & Schlaufman (2015); magenta open pentagons: García-Pérez et al. (2013); grey open pentagons: Howes et al. (2016); grey open pentagons: Koch et al. (2016); green open pentagons: Lamb et al. (2017); green filled circles: Ryde et al. (2016); grey open triangles: Siqueira-Mello et al. (2016); blue open circles: APOGEE original; cyan filled circles: final abundances for the 58 APOGEE sample stars. The lines are the predictions of the chemodynamical models of Friaça & Barbuy (2017) with a formation timescale of 1 Gyr for several radii.

COMBS survey by Lucey et al. (2022). Clearly further investigation on Ce abundances in metal-poor bulge stars is needed.

Ce (Z = 58, A = 140) is essentially an element mostly formed by the s-process, with a fraction of 0.186 as r-element and 0.814 as s-element (Simmerer et al. 2004). Ce appears to be overproduced in massive spinstars (Frischknecht et al. 2016). On the other hand, since we do not have the ages of these stars, we cannot exclude that the Ce enhancement could be due to a mass transfer from a companion Asymptotic Giant Branch (AGB) star (e.g Bisterzo et al. 2011; Cristallo et al. 2015).

5 CONCLUSIONS

We have selected 58 stars from the bulge sample of Queiroz et al. (2021) based on APOGEE with characteristics to belong to the spheroidal pressure-supported bulge. For this sample, we have analysed lines of C, N, O, alpha-elements Mg, Si, Ca, and neutron-capture element Ce. Our fits to the Mg, Si, and Ca abundances from the original APOGEE results using the ASPCAP software appeared to be in good agreement. We recomputed abundances for C, N, O, and Ce, assuming the spectroscopic non-calibrated stellar parameters from APOGEE DR17. We report differences in abundances of these elements.

We compare the abundances of these elements to literature data for bulge stars and chemodynamical models by Friaça & Barbuy (2017) – see also Barbuy et al. (2018a). These comparisons show compatibility of the abundances of the sample stars with literature and models for Mg, Si, and Ca in which a pressure supported component (spheroidal bulge) formed on a very short time-scale (below 1 Gyr). Similar results were suggested by other chemical evolution models

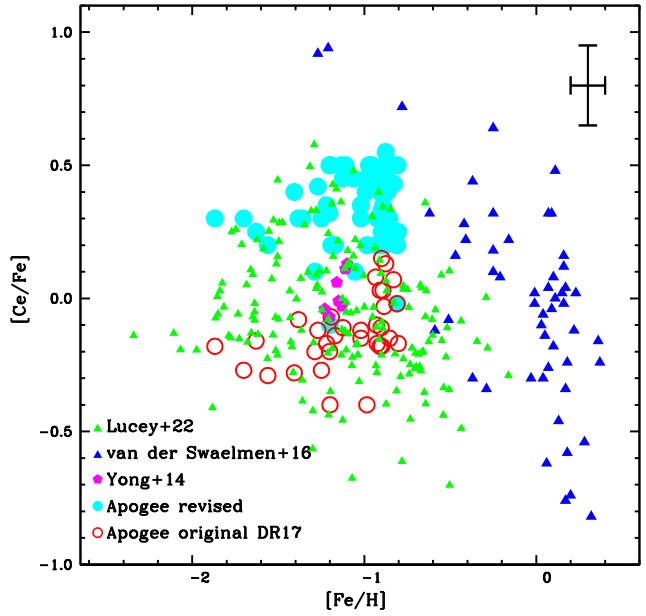

Figure 11. [Ce/Fe] versus [Fe/H] for literature bulge field stars and the APOGEE abundances for the 58 sample stars. Symbols: red filled triangles: van der Swaelmen et al. (2016); green filled triangles: Lucey et al. (2022); magenta pentagons: M62 from Yong et al. (2014); open blue circles: APOGEE DR17 [Ce/Fe] values and cyan filled circles: revised abundances for the 58 APOGEE sample stars. Error bars are indicated in the right upper corner.

(see Matteucci 2021 for a review), and for stars with similar alpha element enhancements with asteroseismic ages (Miglio et al. 2021).

Nitrogen abundances show no exceptional enhancement for any of the sample stars therefore, there is no evidence for these stars to be a result of multiple stellar populations in dissolved globular clusters. The Ce abundance is enhanced in all stars, which would point out to a s-process origin of this element already in the very early phases of chemical enrichment. This could have been achieved with spinstars (e.g. Chiappini et al. 2011; Frischknecht et al. 2016), or alternatively due to mass transfer from a companion AGB star (e.g. Cristallo et al. 2015). This same conclusion was reached by Barbuy et al. (2009, 2014, 2021b) regarding the globular cluster NGC 6522, but here, since all the present sample stars are enhanced in Ce, all of them would have to be binaries with an AGB companion. Therefore the spinstars seem to be a more plausible explanation.

ACKNOWLEDGEMENTS

RR acknowledges a CNPq master fellowship. TM acknowledges FAPESP postdoctoral fellowship no. 2018/03480-7. HE acknowledges a CAPES PhD fellowship. A.P.-V. and S.O.S. acknowledge the DGAPA-PAPIIT grant IA103122. SOS acknowledges a FAPESP PhD fellowship no. 2018/22044-3. SOS and MV acknowledge the support of the Deutsche Forschungsgemeinschaft (DFG, project number: 428473034). BB acknowledges grants from FAPESP, CNPq, and CAPES – Financial code 001. J.G.F-T gratefully acknowledges the grant support provided by Proyecto Fondecyt Iniciación No. 11220340, and also from ANID Concurso de Fomento a la Vinculación Internacional para Instituciones de Investigación Regionales (Modalidad corta duración) Proyecto No. FOVI210020, and from the ESO – Government of Chile Joint Committee 2021 (ORP 023/2021). D.G. gratefully acknowledges support from the ANID BASAL project ACE210002. D.G. also acknowledges financial support from the Dirección de Investigación y Desarrollo de la Universidad de La Serena through the Programa de Incentivo a la Investigación de Académicos (PIA-DIDULS). The work of V.M.P. is supported by NOIRLab, which is managed by the Association of Universities for Research in Astronomy (AURA) under a cooperative agreement with the National Science Foundation. MZ was funded by ANID FONDECYT Regular 1191505, ANID Millennium Institute of Astrophysics (MAS) under grant ICN12_009, the ANID BASAL Center for Astrophysics and Associated Technologies (CATA) through grants AFB170002, ACE210002 and FB210003. DM gratefully acknowledges support by the ANID BASAL projects ACE210002 and FB210003 and by Fondecyt Project No. 1220724. RR, BB, TM, HE, SOS, are part of the Brazilian Participation Group (BPG) in the Sloan Digital Sky Survey (SDSS), from the Laboratório Interinstitucional de e-Astronomia – LIneA, Brazil. Funding for the Sloan Digital Sky Survey IV has been provided by the Alfred P. Sloan Foundation, the U.S. Department of Energy Office of Science, and the Participating Institutions. SDSS acknowledges support and resources from the Center for High-Performance Computing at the University of Utah. The SDSS web site is www.sdss.org. SDSS is managed by the Astrophysical Research Consortium for the Participating Institutions of the SDSS Collaboration including the Brazilian Participation Group, the Carnegie Institution for Science, Carnegie Mellon University, Center for Astrophysics | Harvard & Smithsonian (CfA), the Chilean Participation Group, the French Participation Group, Instituto de Astrofísica de Canarias, The Johns Hopkins University, Kavli Institute for the Physics and Mathematics of the Universe (IPMU) / University of Tokyo, the Korean Participation Group, Lawrence Berkeley National Laboratory, Leibniz Institut für Astrophysik Potsdam (AIP), Max-Planck-Institut für Astronomie (MPIA Heidelberg), Max-Planck-Institut für Astrophysik (MPA Garching), Max-Planck-Institut für Extraterrestrische Physik (MPE), National Astronomical Observatories of China, New Mexico State University, New York University, University of Notre Dame, Observatório Nacional / MCTI, The Ohio State University, Pennsylvania State University, Shanghai Astronomical Observatory, United Kingdom Participation Group, Universidad Nacional Autónoma de México, University of Arizona, University of Colorado Boulder, University of Oxford, University of Portsmouth, University of Utah, University of Virginia, University of Washington, University of Wisconsin, Vanderbilt University, and Yale University. This work makes use of data from the European Space Agency (ESA) space mission Gaia. The Gaia mission website is https://www.cosmos.esa.int/gaia. The Gaia archive website is https://archives.esac.esa.int/gaia.

DATA AVAILABILITY

The observed data are from the APOGEE survey. The calculations and fits to the lines can be requested to the authors. The code for spectrum synthesis is available to be retrieved.

REFERENCES

Abdurro'uf et al., 2022, ApJS, 259, 35
Ahumada R. et al., 2020, ApJS, 249, 3
Alves-Brito A., Meléndez J., Asplund M., Ramírez I., Yong D., 2010, A&A, 513, A35
Arentsen A. et al., 2020, MNRAS, 491, L11
Ashok A. et al., 2021, AJ, 161, 167
Babusiaux C., 2016, PASA, 33, 026
Babusiaux C. et al., 2010, A&A, 519, A77

Barbuy B., Zoccali M., Ortolani S., Hill V., Minniti D., Bica E., Renzini A., Gómez A. 2009, A&A, 507, 405
Barbuy B. et al., 2014, A&A, 570, A76
Barbuy B. et al., 2015, A&A, 580, A40
Barbuy B., Chiappini C., Gerhard O., 2018a, ARA&A, 56, 223
Barbuy B., Trevisan J., de Almeida A., 2018b, PASA, 35, 46
Barbuy B. et al., 2021a, A&A, 648, A16
Barbuy B. et al., 2021b, A&A, 654, A29
Beaton R. L. et al., 2021, AJ, 162, 302
Beers T. C., Christlieb N., 2005, ARA&A, 43, 531
Beers T. C. et al., 2017, ApJ, 835, 81
Belokurov V., Erkal D., Evans N. W., Koposov S. E., Deason A. J., 2018, MNRAS, 478, 611
Bensby T. et al., 2013, A&A, 549, 147
Bensby T. et al., 2017, A&A, 605, 89
Bica E., Ortolani S., Barbuy B., 2016, PASA, 33, e028
Bisterzo S., Gallino R., Straniero O., Cristallo S., Käppeler F., 2011, MNRAS, 418, 284
Blanton M. R. et al., 2017, AJ, 154, 28X
Casey A. R., Schlaufman K. C., 2015, ApJ, 809, 110
Chiappini C., Frischknecht U., Meynet G., Hirschi R., Barbuy B., Pignatari M., Decressin T., Maeder A., 2011, Nature, 474, 666
Cristallo S., Straniero O., Piersanti L., Gobrecht D., 2015, ApJS, 219, 40
Cunha K., Smith V. V., 2006, ApJ, 651, 491
Cunha K. et al., 2017, ApJ, 844, 145
Debattista V. P., Ness M., Gonzalez O.A, Freeman K., Zoccali M., Minniti D., 2017, MNRAS, 469, 1587
Dékány I., Minniti D., Catelan M., Zoccali M., Saito R. K., Hempel M., Gonzalez O. A., 2013, ApJ, 776, L19
Duong L., Asplund M., Nataf D. M., Freeman K. C., Ness M., Howes L. M., 2019a, MNRAS, 486, 3586
Duong L., Asplund M., Nataf D. M., Freeman K. C., Ness M., 2019b, MNRAS, 486, 5349
Fanelli C., Origlia L., Oliva E., Mucciarelli A., Sanna N., Dalessandro E., Romano D., 2021, A&A, 645, A19
Fernández-Trincado J. G. et al., 2020a, A&A, 643, A145
Fernández-Trincado J. G. et al., 2020b, ApJ, 903, L17
Fernández-Trincado J. G., Beers T. C., Barbuy B. et al., 2022, A&A, 663, A126
Ferraro F. R. et al., 2021, NatAs, 5, 311
Friaça A. C. S., Barbuy B., 2017, A&A, 598, A121
Frischknecht U. et al., 2016, MNRAS, 456, 1803
Fulbright J. P., McWilliam A., Rich R. M., 2007, ApJ, 661, 1152
Gaia Collaboration et al., 2021, A&A, 649, A1
García-Pérez A. et al., 2013, ApJ, 767, L9
García-Pérez A. E. et al., 2016, AJ, 151, 144
Goldman A., Schoenfeld W. G., Goorvitch D., Chakerian C., Jr., Dothe H., Mélen F., Abrams M. C., Selby J. E. A., 1998, J. Quant. Spec. Radiat. Transf., 59, 453
Goorvitch D., 1994, ApJS, 95, 535
Gratton R. G., Sneden C., 1990, A&A, 234, 366
Grevesse N., Sauval J. N., 1998, SSRev, 35, 161
Grevesse N., Noels A., Sauval J., 1996, ASP, 99, p. 117
Grevesse N., Scott P., Asplund M., Sauval A. J., 2015, A&A, 573, 25
Gunn J. E. et al., 2006, AJ, 131, 2332
Gustafsson B., Edvardsson B., Eriksson K., Jørgensen U. G., Nordlund B., Plez Å., 2008, A&A, 486, 951
Hasselquist S. et al., 2016, ApJ, 833, 81
Helmi A., Babusiaux C., Koppelman H. H., Massari D., Veljanoski J., Brown A. A. G., 2018, Nature, 563, 85
Hill V. et al., 2011, A&A, 534, A80
Hinkle K. H., Wallace L., Livingston W., 1995, Infrared Atlas of the Arcturus Spectrum, 0.9-5.3 microns. ASP, San Francisco
Horta D. et al., 2020, MNRAS, 493, 3363
Horta D. et al., 2021, MNRAS, 500, 1385
Horta D. et al., 2022, MNRAS, in press? (arXiv:220404233H)
Howes L. M. et al., 2016, MNRAS, 460, 884
Iwamoto K., Brachwitz F., Nomoto K., Kishimoto N., Umeda H., Hix R. W., Thielemann F., 1999, ApJS, 125, 439
Ji A. P., Frebel A., Anirudh C., Simon J., 2016, Nature, 531, 610
Johnson C. I., Rich R. M., Kobayashi C., Kunder A., Koch A., 2014, AJ, 148, 67
Jönsson H., Ryde N., Schultheis M., Zoccali M., 2017, A&A, 600, 2
Jönsson H., Allende Prieto C., Holtzman J. A., 2018, AJ, 156, 126
Jorgensen U. G., 1994, A&A, 284, 179
Kerber L. et al., 2019, MNRAS, 484, 5530
Koch A., McWilliam A., Preston G. W., Thompson I. B., 2016, A&A, 587, 124
Kunder A. et al., 2020, AJ, 159, 270
Kurucz R., 1993, CD-ROM 23
Lamb M. et al., 2017, MNRAS, 465, 3536
Lecureur A., Hill V., Zoccali M., Barbuy B., G´omez A., Minniti D., Ortolani S., Renzini A., 2007, A&A, 465, 799
Lodders K., Palme H., Gail H.-P., 2009, Solar System, Landolt-Börnstein - Group VI Astronomy and Astrophysics, Volume 4B. ISBN978-3-540-88054-7. Springer-Verlag, Berlin, Heidelberg, p. 712
Lucey M. et al., 2019, MNRAS, 488, 2283
Lucey M. et al., 2021, MNRAS, 501, 5981
Lucey M. et al., 2022, MNRAS, 509, 122
Majewski S. R., Schiavon R. P., Frinchaboy P. M., 2017, AJ, 154, 94
Martin W. C., Fuhr J. R., Kelleher D. E., Musgrove A., Sugar J., Wiese W. L., Mohr P. J., Olsen K. J., 2002, NIST Atomic Database (version 2.0), 'http://physics.nist.gov/asd'. National Institute of Standards and Technology, Gaithersburg, MD
Matteucci F., 2021, A&ARv, 29, 5
McWilliam A., 2016, PASA, 33, 40
Meléndez J., Barbuy B., 1999, ApJS, 124, 527
Meléndez J., Barbuy B., Spite F., 2001, ApJ, 556, 858
Meléndez J., Barbuy B., Bica E., Zoccali M., Ortolani S., Renzini A., Hill V., et al., 2003, A&A, 411, 417
Miglio A. et al., 2021, A&A, 645, A85
Minniti D. et al., 2017, AJ, 153, 179
Nidever D. L. et al., 2015, AJ, 150, 173
Nomoto K., Kobayashi C., Tominaga N., 2013, ARA&A, 51, 457
Ortolani S. et al., 2019, A&A, 627, A145
Osorio Y., Allende Prieto C., Hubeny I., Mészáros Sz., Shetrone M., 2020, A&A, 637, A80
Pérez-Villegas A., Barbuy B., Kerber L., Ortolani S., Souza S. O., Bica E., 2020, MNRAS, 491, 3251
Piskunov N., Kupka F., Ryabchikova T., Weiss W., Jeffery C., 1995, A&AS, 112, 525
Portail M., Wegg C., Gerhard O., 2015, MNRAS, 450, L66
Queiroz A. B. A. et al., 2018, MNRAS, 476, 2556
Queiroz A. B. A. et al., 2020, A&A, 638, A76
Queiroz A. B. A. et al., 2021, A&A, 656, A156
Ramírez I., Allende Prieto C., 2011, ApJ, 743, 136
Rojas-Arriagada A. et al., 2017, A&A, 601, A140
Rojas-Arriagada A. et al., 2020, MNRAS, 499, 1037
Rossi L., Ortolani S., Barbuy B., Bica E., Bonfanti A., 2015, MNRAS, 450, 3270
Ryabchikova T., Piskunov N., Kurucz R. L., Stempels H. C., Heiter U., Pakhomov Y., Barklem P. S., 2015, PhyS, 90, 054005
Ryde N. et al., 2010, A&A, 509, A20
Ryde N., Schultheis M., Grieco V., Matteucci F., Rich R. M., Uttenthaler S., 2016, AJ, 51, 1
Santana F. A. et al., 2021, AJ, 162, 303
Santiago B. X. et al., 2016, A&A, 585, 42
Savino A., Koch A., Prudil Z., Kunder A., Smolec R., 2020, A&A, 641, A96
Schiavon R. P., Barbuy B., 1999, ApJ, 510, 934
Schiavon R. P. et al., 2017, MNRAS, 465, 501
Scott P., Asplund M., Grevesse N. Bergemann M., Sauval J. A., 2015a, A&A, 573, A26
Scott P. Asplund M., Grevesse N. A. Sauval J. 2015b, A&A, 573, A27
Shetrone M. et al., 2015, ApJS, 221, 24

Simmerer J., Sneden C., Cowan J. J., Collier J., Woolf V. M., Lawlwr J. E., 2004, ApJ, 617, 1091
Siqueira-Mello C. et al., 2016, A&A, 593, A79
Smith V. V. et al., 2013, ApJ, 765, 16
Smith V. et al., 2021, AJ, 161, 254
Souza S. O. et al., 2021, A&A, 656, A78
Timmes F. X., Woosley S. E., Weaver T. A., 1995, ApJS, 98, 617
Tumlinson J., 2010, ApJ, 708, 1398
van den Hoek L. B., Groenewegen M. A. T., 1997, A&A, 123, 305
van der Swaelmen M., Barbuy B., Hill V., Zoccali M., Minniti D., Ortolani S., Gómez A., 2016, A&A, 586, A1
Wilson J. C. et al., 2019, PASP, 131, e5001
Wise J. H., Turk M. J., Norman M. L., Abel T., 2012, ApJ, 745, 50
Woosley S. E., Weaver T. A., 1995, ApJS, 101, 181
Yong D. et al., 2014, MNRAS, 439, 2638

Zasowski G. et al., 2013, AJ, 146, 81
Zasowski G. et al., 2017, AJ, 154, 198
Zasowski G. et al., 2019, ApJ, 870, 138
Zoccali M. et al., 2006, A&A, 457, L1
Zoccali M., Valenti E., Gonzalez O. A., 2018, A&A, 618, A147

This paper has been typeset from a TEX/LATEX file prepared by the author.